AD-A123 297 CAVITATION PHENOMENON IN FACE SEALS(U) NORTHWESTERN 1/1
UNIV EVANSTON IL DEPT OF MECHANICAL AND NUCLEAR
ENGINEERING A L KISTLER ET AL. 15 JUL 81
UNCLASSIFIED N00014-79-C-0007 F/G 20/4 NL

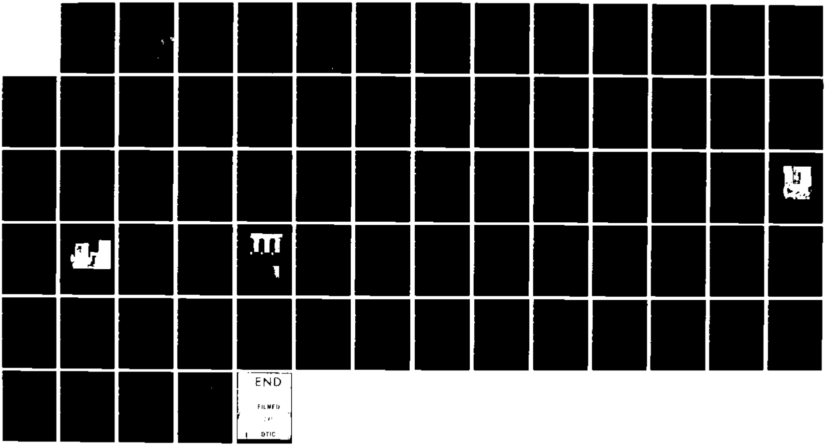

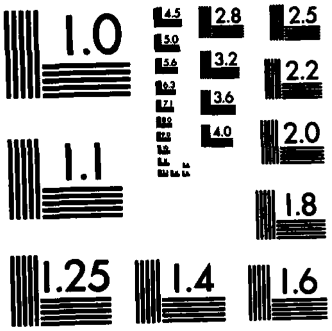
1.0
4.5
5.0
5.6
6.3
7.1
8.0
2.8
3.2
3.6
4.0
2.5
2.2
2.0
1.1
1.8
1.25
1.4
1.6

① No DTIC 7/82

AD A123297

CAVITATION PHENOMENON IN FACE SEALS

BY

A. L. KISTLER, H. S. CHENG, K. NIVATVONGS and I. ÖZAKAT

Department of Mechanical and Nuclear Engineering

Northwestern University

Evanston, Illinois 60201

DTIC
ELECTE
JAN 11 1983
S D
H

Prepared for Office of Naval Research under

ONR Contract No. N00014-79-C-0007

DTIC FILE COPY

83 01 11 063

REPORT DOCUMENTATION PAGE

READ INSTRUCTIONS
BEFORE COMPLETING FORM

1. REPORT NUMBER

2. GOVT ACCESSION NO. AD-A113297

3. RECIPIENT'S CATALOG NUMBER

4. TITLE (and Subtitle)
Cavitation Phenomenon in Face Seals

5. TYPE OF REPORT & PERIOD COVERED
Final Report, Oct. 1, 1978
to Sept. 30, 1980

6. PERFORMING ORG. REPORT NUMBER

7. AUTHOR(s)
A. L. Kistler, H. S. Cheng, K. Nivatvongs, and
I. Özakat

8. CONTRACT OR GRANT NUMBER(s)
N00014-79-C-0007

9. PERFORMING ORGANIZATION NAME AND ADDRESS
Department of Mechanical & Nuclear Engineering
Northwestern University
Evanston, IL 60201

10. PROGRAM ELEMENT, PROJECT, TASK AREA & WORK UNIT NUMBERS
NR091-009/9-05-79(473)

11. CONTROLLING OFFICE NAME AND ADDRESS
Procuring Contacting Officer
Office of Naval Research - Dept. of the Navy
Arlington, VA 22217

12. REPORT DATE
July 15, 1981

13. NUMBER OF PAGES
67

14. MONITORING AGENCY NAME & ADDRESS (if different from Controlling Office)

15. SECURITY CLASS. (of this report)
Unclassified

15a. DECLASSIFICATION/DOWNGRADING SCHEDULE

16. DISTRIBUTION STATEMENT (of this Report)

Reproduction in whole or in part is permitted for any purpose of the United States Government.

APPROVED FOR PUBLIC RELEASE
DISTRIBUTION UNLIMITED

17. DISTRIBUTION STATEMENT (of the abstract entered in Block 20, if different from Report)

18. SUPPLEMENTARY NOTES

19. KEY WORDS (Continue on reverse side if necessary and identify by block number)

Cavitation, Seals, Tribology, Lubrication, Surface Roughness.

20. ABSTRACT (Continue on reverse side if necessary and identify by block number)

An experimental rig consisting of a hydrostatic circular step pad was constructed to simulate the cavitation phenomenon under a water pressure up to 2000 psi comparable to those in the submarine stern-tube seals. Cavitation bubbles were observed for water glycerine, and their mixtures.

Several analytical models were studied, and the physical parameters influencing bubble growth and collapse were identified. An analysis was also

DD FORM 1473 1 JAN 73 EDITION OF 1 NOV 65 IS OBSOLETE
S/N 0102-LF-014-6601

20. (cont.)

made to determine the axisymmetric stress in the solid induced by a sudden pressure distribution during the collapsing of a bubble.

An existing thin-film analysis for determining the flow factors used in the hydrodynamic analysis of rough surfaces was extended to include the steady-state cavitation effects. Results showed that the shear flow factors ϕ_s^* calculated using a model considering cavitation are dependent on ambient pressure, surface pattern parameter and the film thickness to roughness ratio, h/σ.

The model predicts a lower shear flow factor when cavitation is considered. They approach asymptotically to the non-cavitated values as the ambient pressure rises. The effect of cavitation are found to be less significant for $h/\sigma > 3$or for $h/\sigma > 0.75$ and more significant for the intermediate values. The surfaces with transverse roughness resulted in more cavitated regions than isotropic and longitudinal roughness.

TABLE OF CONTENT

ABSTRACT

An experimental rig consisting of a hydrostatic circular step pad was constructed to simulate the cavitation phenomenon under a water pressure up to 2000 psi comparable to those in the submarine stern-tube seals. Cavitation bubbles were observed for water glycerine, and their mixtures.

Several analytical models were studied, and the physical parameters influencing bubble growth and collapse were identified. An analysis was also made to determine the axisymmetric stress in the solid induced by a sudden pressure distribution during the collapsing of a bubble.

An existing thin-film analysis for determining the flow factors used in the hydrodyamic analysis of rough surfaces was extended to include the steady-state cavitation effects. Results showed that the shear flow factors ϕ_s^* calculated using a model considering cavitation are dependent on ambient presure, surface pattern parameter and the film thickness to roughness ratio, h/σ .

The model predicts a lower shear flow factor when cavitation is considered. They approach asymptotically to the non-cavitated values as the ambient pressure rises. The effect of cavitation are found to be less significant for $h/\sigma > 3$ or for $h/\sigma > 0.75$ and more significant for the intermediate values. The surfaces with transverse roughness resulted in more cavitated regions than isotropic and longitudinal roughness.

I. INTRODUCTION

In high pressure face seals, such as the submarine stern-tube seals, it is often found from the prematurely failed seals that sections of the seal surface show a matted appearance similar to the surfaces damaged by cavitation (1). This mode of failure appears to be even more prevalent as both the pressure differential and the seal size are enlarged. It has been suggested that such surface damage may be caused by the collapsing of cavitated bubbles associated with the sudden drop in pressure in a rapidly diverging channel. In order to understand the basic mechanism of cavitation damage in a narrow gap between the sealing surfaces, a research program was initiated at Northwestern to meet the following objectives:

a) Design and construct an experiment to simulate the cavitation phenomenon under conditions comparable to those in the recent high pressure-stern-tube seals.

b) To formulate an analytical model to explain the growth and collapse of the cavitating bubbles in a narrow film.

c) To employ an existing thin-film analysis for rough surface to predict the effect of cavitation on the steady-state performance between sliding sealing surfaces.

This report presents the results obtained during the first phase of the above described tasks.

II. CAVITATION IN FACE SEALS

Mechanical seals consist of two surfaces in relative motion and in intimate contact. The gap between the parts is of the order of the surface irregularities (typically a fraction of a micrometer). The formation and collapse of vapor bubble in the fluid that fills the thin sealing gap is known as cavitation in face seals.

Cavitation in external flows; e.g., around propellers or moving objects immersed in water, involves vapor bubbles growing in the liquid at low pressure regions, and subsequently collapsing when exposed to a higher pressure. Experiments have shown these bubbles start as nuclei in the water of about 1 micrometer in size (2). Nuclei of this size in a seal gap must grow into disk shaped vapor bubbles because of the constraining surfaces. The fundamental geometry is cylindrical rather then spherical (Fig. 1 illustrates this difference).

Cavitation damage to solid surfaces is associated with vapor bubbles collapsing in the neighborhood of the surface (3). In order to explain cavitation damage in seals, it is necessary to establish how vapor bubbles grow and collapse in the gap region. A bubble must grow to a certain size before its collapse can generate enough disturbance to cause damage.

Several paths can produce this history for a bubble. The most direct occurs when the bubble remains stationary in the fluid and the local pressure first decreases and then increases. Such a pressure history might be generated by squeeze film action if the gap between the two surfaces periodically changes (due to vibration or other dynamical effects). For unconfined flows cavitation is produced in this manner by ultrasonic generators. Unsteady pressure fields such as these are also produced by roughness on the two surfaces. As asperities pass one another, the neighboring fluid is subjected to a time varying pressure field.

Another path is through convection, wherein a bubble is formed in a low pressure region and is then transported by the fluid to a region where the pressure is higher. A typical example of this process for unconfined flows occurs on submerged bodies where vapor bubbles originate at low pressure shoulder regions and collapse when transported to a reattachment region (4).

An important question in this case is how a steady flow produces an unsteady flow of bubbles. Turbulence plays a role as well as the stability properties of the interface between the vapor and liquid. The incompatability of the constant pressure vapor filled region and the adjacent liquid flow which requires pressure changes along the boundary is also important (5). This latter effect might also be important in the seal problem, whereas turbulence and interfacial instability are unlikely to be of importance because of the characteristically low Reynolds number for seal flows.

III. STEADY VAPOR BUBBLES IN SEAL FLOW

The flow in the seal gap satisfies the same equations as the flow in journal bearings. If only one seal surface is rough, the flow satisfies (6)

$$\frac{\partial}{\partial x}\left(\frac{h^3}{12\mu}\frac{\partial P}{\partial x}\right) + \frac{\partial}{\partial y}\left(\frac{h^3}{12\mu}\frac{\partial P}{\partial y}\right) = 6U\frac{\partial h}{\partial x} \quad , \tag{1}$$

where P is the local pressure, x, y are cartesian coordinates in the plane of the surface, h is the variable spacing between the surfaces, μ is the viscosity, and U is the local velocity of the smooth surface in a coordinate system where the rough surface is at rest. The local average fluid velocities are

$$u_x = -\frac{h^2}{12\mu}\frac{\partial P}{\partial x} + \frac{Uh}{2} \tag{2}$$

$$u_y = -\frac{h^2}{12\mu}\frac{\partial P}{\partial y} \tag{3}$$

We ask the question whether a steady vapor bubble is possible in the flow described by these equations? These equations do not include details of the bubble shape in the third dimension. The effect of this can be accounted for to some degree of approximation by imposing a pressure jump across the vapor-liquid interface equal to the product of the surface tension and the curvature. For a steady vapor bubble, the requirement at the interface is that the pressure is constant, and that the interface is a stream line. The bubble must also be a local minimum of pressure, so that the pressure must rise as one moves away from the bubble. This pressure gradient always drives the liquid toward the vapor bubble. The moving boundary always tries to carry the liquid in the direction of its motion. These two forces can be in balance for a streamline-bubble boundary only if the normal direction of the bubble surface in the direction from the vapor to the liquid has a component in the direction of the motion of the moving boundary. This implies that the only steady bubbles which are possible are those whose upstream surface is a solid asperity that excludes the fluid (h=0). Separation of the flow into vapor and liquid layers in the third dimension is not likely in the steady state unless the vapor in composed of a permanent gas.

If the solution of Eq. (1) gives a pressure less than the vapor pressure of the liquid, and the conditions stated above are not met, the flow must violate the equation either by becoming unsteady or by developing a strong three dimensional component. Perhaps convected bubbles appear which can be carried to high pressure regions where they collapse.

For flows where steady vapor bubbles are assumed to exist, the pressure distribution on the surface is different than that which would exist if no bubbles were present. Calculations of the effect of this steady cavitation on the leakage rate and the forces on a seal surface are presented in Section VII.

IV. BUBBLE DYNAMICS IN CONFINED SPACES

Some idea of the possible pressures that can be produced by bubble collapse in the seal gap can be obtained by examining limiting forms of the equations of motion for bubble growth. The inviscid limit is appropriate when changes occur so rapidly that viscous shears do not have time to diffuse across the gap. In this limit, the dynamic equation for a bubble in a constant thickness gap can be obtained by a simple extension of the equation for a spherical bubble in an infinite space (7). For the limit that the bubble radius is much greater than the gap thickness, the equation is

$$P \ln \frac{r'}{R} \left(R \frac{dU}{dt} + U^2 \right) = \frac{NT}{R^2} - \frac{2\sigma}{h} - \left(P_\infty - P_v \right) \quad . \tag{4}$$

Here R is the radius of the disk shaped bubble, U is dR/dt, r' is some outer boundary at a distance much greater than R, h is the gap thickness, σ is the surface tension constant, P_v is the vapor pressure of the liquid, p_∞ is the fluid pressure at large distances from the bubble, ρ is the fluid density, and NT is related to the amount of inert gas within the bubble. Values of R and $(P_\infty - P_v)$ which make the right hand side equal to zero are possible equilibrium sizes for a given nucleus. Figure 2 shows this relation graphically. For a given NT, there is some pressure below which no equilibrium size can exist. For values of R, $(P_\infty - P_v)$ off the equilibrium curve, Eq. (4) shows how R changes with time. If we define

$$R_o = \left(\frac{NT}{\frac{2\sigma}{h} + \left(P_\infty - P_v \right)} \right)^{1/2} \quad , \quad R' = \frac{R}{R_o} \quad , \quad \tau_o^2 = \frac{\rho R_o^4}{NT} \quad , \quad t' = \frac{t}{\tau_o} \quad ,$$

the equation can be written

$$\ln \left(\frac{r'}{R} \right) \left[R' \frac{d^2 R'}{dt'^2} + \left(\frac{dR}{dt} \right)^2 \right] = \left(\frac{1}{R'^2} - 1 \right) + \frac{P_\infty}{\rho} \frac{\tau_o^2}{R_o^2} \tag{5}$$

τ_o and R_o are characteristic length and time scales. The solution of this equation for two different pressure histories are shown in Fig. 3 and Fig. 4. In Fig. 3 the change in R for a step increase in pressure is shown. The initial conditions were that R is an equilibrium value at $t' = 0$, and $dR/dt = 0$. A step increase in pressure is applied and R is seen to oscillate with a period dependent on the size of the pressure jump. In Fig. 4, a low pressure is first applied so that the bubble grows, and then a high pressure is applied. Here, the bubble collapses to zero size. This behavior is similar to that of a spherical bubble and is known to lead to high pressures and cavitation damage to surfaces. This type of behavior arises from inertia effects that are represented by the U^2 terms in the dynamical equation.

The other limiting case for bubble growth corresponds to such slow changes, that viscous forces balance the pressure forces and the inertia is of no importance.

For this limit, the flow in the neighborhood of the liquid-vapor interface presents some difficulties. A complex interaction of surface tension, viscous stresses, and pressure determine the interface shape, the thickness of the fluid layer adhering to the solid surfaces, and the pressure changes in the neighborhood of the bubble (8,9). A qualitative view of the flow in this limit can be obtained by balancing the bubble pressure with a quasi-static viscous flow. An approximate equation is

$$\frac{12\mu}{h^2} \ln \frac{r'}{R} RU = \frac{NT}{hR^2} - \frac{2\sigma}{h} - \left(P_\infty - P_v\right) \qquad (6)$$

This equation does not have the non-linear terms that gave the solutions of the inviscid equation their violent behavior on collapse. If the flow in seal gaps is controlled to a good approximation by this equation, then the rapid collapse of bubbles leading to cavitation damage is not likely. The time scale for growth and collapse becomes the crucial element in determining which type of flow field will exist, and the physical basis for estimating this becomes the goal of this work.

V. STRESSES IN THE SOLID

Cavitation damage results from the stresses applied to the solid surface by the flow field associated with a collapsing bubble. For extended flows only a small fraction of the collapsing bubbles produce damage (10). This is thought to be due to the requirements that damaging collapse must occur near the surface, and also must be of the type (asymmetric) and orientation that can cause damage. These two requirements strongly restrict the number of damaging blows.

Cavitation in a gap always occurs in close proximity to the surface and only one type of collapse is likely. If damaging collapse occurs at all, it is likely that almost every bubble will produce damage.

The stresses in a solid produced by an axisymmetric distribution of pressure on the surface can be computed within the elastic limit by existing theory (11). Knowledge of the pressure field generated by the fluid motion will easily lead to an assessment of its damage producing potential. The shear stress on the axis produced by two different distirbutions of surface pressure is shown in Fig. 5. One is for a uniform pressure within a circle, and the other is for a ring shaped distribution. The latter distribution is more typical of that associated with bubble collapse. In both examples, the shear stress on the axis is maximum at a short distance below the surface, and is a fraction of the surface pressure. Other distributions of pressure give similar results.

VI. EXPERIMENTAL PROGRAM

An apparatus was constructed that could produce cavitation in a seal like gap, and where the bubble growth and collapse process could be produced in a controlled and observable manner.

The Rig

A drawing of the rig test area is shown in Fig. 6. A flat or shaped test surface ((4) in Fig. 6) 25.4 mm in diameter is held against a flat, transparent quartz disk ((5) in Fig. 6) by a hydraulic cylinder. The test surface is mounted so that it can remain parallel to the quartz surface. A load cell ((7)) supports the quartz and measures the force applied to the surface. The force between the disk and the surface can be varied in time with a frequency up to 200 Hz and with an amplitude of the steady component plus the oscillating component of up to 2000 lbs (8910N). The test surface has a central hole through which liquid can be forced with a pressure up to 2000 psi (13.8×10^6 Pa). A photograph of the test area is shown in Fig. 7.

The hydraulic cylinder, and load cell are part of the closed loop drive system shown schematically in Fig. 8. A voltage into the input module causes a force to be applied to the test surface with the same time variation as the voltage and with a level proportional to the voltage. An MTS "SERVAC" controller is used. An overall view of the test facility is shown in Fig. 9.

Test Procedure

The test surface is held so that it remains parallel to the transparent surface. An inverted microscope permits observation and photography of the interface between the disk and test surface by looking through the flat quartz disk.

A proximity probe (Bentley-Nevada) imbedded in the quartz senses the motion of the test surface. A pressure transducer whose face can be lapped flush with the test surface is being installed in the test piece.

For normal operation, a test surface is made with a stepped surface as shown in Fig. 10. The surface can be examined with a tallysurf profilometer to verify its shape. By changing the liquid pressure and applied steady force, the average gap size can be set over a limited range. The pressure distributions associated with three different gap sizes are also shown in Fig. 10, each with a different shape corresponding to a different total force related to the pressure integral. If this steady force is modified by an oscillating force, the pressure distribution and gap will vary accordingly, and the desired negative pressures can be produced in a region of the gap for part of the cycle. Figure 11 shows three instantaneous pressure distributions for different parts of a cycle - when the surfaces are approaching one another, when they are separating, and when they are at rest. The velocities shown correspond to a 30 Hz oscillation with an amplitude of about half the initial gap.

The negative pressure region occuring when the plates are separating (or when upper surface is moving upward) is the region where cavitation is expected to occur. The process of bubble growth and collapse in this region can be observed and serve as a basis for evaluating the various theoretical models.

Results

The apparatus has gone through several generations of change, and is now rigid enough and with sufficient degrees of freedom, to enable it to perform as planned. The control of the pressure in the gap by using the force on the surface as the controlled variable has presented some problems, particularly if the force changes sign during part of the cycle. Control by means of local pressure or by relative displacement of the surface is now being investigated and should lead to better defined conditions in the gap.

Some photographs of bubbles produced by the apparatus are shown in Fig. 12. The top picture shows several frames of a motion picture take through a microscope at 1000 frames/seconds of bubbles forming and collapsing in glycerin. The large viscosity of glycerin slows down its motion so that the history of the motion is accessible. The lower picture slows a still picture of bubbles produced in water (1/1000 second exposure). The small viscosity and large surface tension of water makes it more difficult to produce bubbles and also more difficult to follow the details of their history. At this time, all we can say is cavitation bubbles have been produced, but insufficient observations have been obtained with which develop understanding of the cavitation process.

VII. THE FLOW FACTOR AND LOAD CAPACITY FOR CAVITATION MODEL

Introduction

When sliding is introduced in a rough bearing, there is a possibility of cavitation at the trailing edge of the asperities. Cavitation is the result of pressure reductions in the liquid, more precisely, it occurs if the pressure is reduced and maintained for sufficient duration below a certain critical pressure which is determined by the physical properties and conditions of the liquid. The type of cavitation studied in this section is termed steady cavitation; it refers to the time independent situation in which the liquid flow detaches from the rigid boundary of an immersed body.

When a sliding is introduced in a rough bearing, the pressure distribution about each asperity is expected to be antisymmetric. However, due to the fact that the lubricant cannot withstand large negative pressures, it can rupture at the negative pressure zones. There are conflicting views on whether or not this cavitation will always occur. For examples, for some geometrical situations, Burton (12) believes that cavitation voids could not be expected to nucleate in the short time available. However, Hamilton et. al. (13) relates the load support mechanism in face-type or axial seals to the cavitation. They show that the classical lubriction theory does not predict the existence of load support in the case of flat, parallel surfaces which are separated by a uniform, steady film of Newtonian fluids. But, since high positive pressures overcome the negative pressures which are truncated due to the cavities, these types of seals do produce a net load carrying capacity.

In this section, it is assumed that cavitation occurs whenever the fluid pressure drops below the ambient pressure. However, as indicated above, although the pressure drops below the critical pressure, there is some question as to whether cavitation always occurs. Therefore, one should be aware of the fact that this model may under-estimate the shear flow factor in case of cavitation, which tends to reduce shear flow in a bearing.

A typical contact area in a rough bearing and the negative pressure zones is shown in Figure 13. As one may observe, most of the cavitation occurs at the trailing edge of the contacts and the rest occurs at the trailing edge of the asperities.

To analyze the shear flow and load capacity in case of steady cavitation, it is assumed that these negative pressure zones are, in fact, isobaric regions, whose pressure is equal to the vapor pressure of the lubricant. Since the vapor pressure of lubricant is negligible when compared with the pressure build-up in the bearing, it is taken to be zero.

The shear flow factor is calculated by substituting this modified pressure into Equation A-20 (Appear in Appendix A). Finally, the load capacity for the bearing is evaluated using truncated pressure distribution as indicated in the following sections.

Shear Flow Factor

The shear flow factors that are presented in this section are evaluated using model problem 3 as described in Appendix A. The presence of the cavities affects the shear flow in a bearing due to the reduction of the areas where lubricant flows. The existence of a cavity strongly depends on the ambient pressure and sliding speed of the bearing; therefore, the shear flow (ϕ_s^*) becomes a function of ambient pressure and sliding speed as well as h/σ and γ. However, since ϕ_s^* is non-dimensionalized by $\overline{U}_s$, the shear flow factor becomes

$$\phi_s^* = \phi_s^* \, (h/\sigma, \gamma, P_a) \tag{7}$$

The effects produced by these parameters are now discussed. In Figure 14, a typical pressure distribution about an asperity is shown. It is evident also from the figure that as the ambient pressure increases the change of negative pressures near asperity decreases. Therefore, one expects to get higher flows as the ambient pressure rises. The effect of ambient pressure on shear flow for isotropic surfaces is given in Figure 15. It is observed that as the ambient pressure increases, the ϕ_s^* values, evaluated considering cavitation effects, approach asymptotically the shear flow factors without cavitation. This approach of ϕ_s^* becomes much faster for $h/\sigma = 3$ and $h/\sigma = 0.5$. It is slower for the intermediate values.

The faster convergence of shear flow factor ϕ_s^* at high h/σ can be attributed to the offset of the cavitation effects due to the other parameters. At high h/σ values, the volume occupied by cavitation becomes less dominant to the main flow. (In contrast, for small values of h/σ the cavitation effects become more dominant because of an increasing number of contacts in the bearing area.)

Figure 16 shows the change of ϕ_s^* with ambient pressure for isotropic, transverse and longitudinal roughness. It is found that the change in ϕ_s^* is larger for transverse roughness type, that is, cavitation is more pronounced for these types of surfaces. This is mainly due to the fact that the areas behind the asperities which are cavitated are larger than those of isotropic and longitudinal, the fluid must travel a longer distance to fill the cavities at the trailing edges of the asperities.

In Figure 17, the variation of shear flow factor with h/σ for isotropic surfaces is shown. It is found that shear flow factor for the cavitation model behaves the same way as the shear flow factor of the model described in Appendix A for non-cavitating flow. It approaches zero as h/σ increases above 3 due to the vanishing effect of roughness; as h/σ decreases it increases to a certain maximum and then sharply drops towards zero. The reason for this behaviour is due to the increased flow transport in the valleys. The decrease is due to the decrease in flow area because of contacts, as described in Appendix A. However, it is found that the maximum points shift towards high h/σ values as ambient pressure is increased. When cavitation occurs, the flow is reduced due to blockade by cavitated regions and contacts. It is also observed in Figure 15 that for values of h/σ less than 1 cavitation effects are less pronounced compared to $h/\sigma > 1$. Therefore, as h/σ drops below 1, the decrease in flow is compensated by the decrease in cavitation. This is because at low ambient pressures the cavitation is more effective, and compensation becomes more dominant, delaying the shear factor from dropping towards zero.

Figure 18 shows the change of ϕ_s^* with h/σ for transversely and longitudinally oriented roughness. The surfaces with longitudinal roughness result in a lower shear flow than the surfaces with transverse roughness. However, it is clear from the figure that transversely oriented surfaces are more sensible to ambient pressure, since more cavitation occurs for that case.

Load Capacity

The classical lubrication theory does not predict any load support for two parallel, smooth surfaces sliding against each other. For rough surfaces, the pressure distribution about each asperity is anti-symmetric, and the negative pressures cancel the positive pressures. This results in no net load support, even for rough surfaces. However, since is practice the negative pressure regions may be cavitated, rough surfaces can create a net load capacity.

The load capacity in a bearing is given by

$$w = \int_o^{L_x} \int_o^{L_y} p^* dxdy \tag{8}$$

where p^* is the truncated pressure distribution. Defining non-dimensional pressure and load as

$$W = \frac{h^2}{6\mu U_s L_x^2 L_y} w \quad , \quad P^* = \frac{h^2}{6\mu U_s L_x} p^* \tag{9}$$

Equation (8) becomes

$$W = \int_o^1 \int_o^1 P^* \, d\bar{x}d\bar{y} \tag{10}$$

The results calculated using Eq. (10) are shown in Figure 19.

Conclusions

1. The shear flow factors ϕ_s^* calculted using a Model considering cavitation (Model 3 in Appendix A) are found to be dependent on ambient pressure as well as surface pattern parameter and h/σ . The ϕ_s^* increases as P_a increases, and otherwise, exhibits the same behaviour as the non-cavitated model with respect to changes in h/σ and γ.
2. The model predicts a lower shear flow factor when cavitation is considered. They approach asymptotically to the non-cavitated values as the ambient pressure rises.

3. The effect of cavitation is found to be less significant for $h/\sigma > 3$ or for $h/\sigma > 0.75$ and more significant for the intermediate values.

4. The surfaces with transverse roughness resulted in more cavitated regions than isotropic and longitudinal roughness.

VIII. COMPARISON OF FLOW FACTORS FOR GAUSSIAN SURFACES BETWEEN THE OPEN AND CLOSED BOUNDARY MODELS

Introduction

In this section, the flow factors obtained through simulation are presented. Although one may use any kind of surface roughness, it is impossible to consider every possible roughness configuration within the scope of this study. Therefore, only the Gaussian surfaces as suggested by Patir and Cheng (14) have been used to facilitate a direct comparison with their results. Most of the roughness parameters of a surface can be obtained from two statistical functions: the frequency density of roughness heights and the auto-correlation function of the surface. Therefore, a convenient way to characterize surfaces would be to choose specific functions to approximate real surfaces. The frequency density of the surfaces used is chosen such that it can be approximated by Gaussian frequency density function, and the auto-correlation function of the surfaces is chosen such that it results in linear auto-correlation functions for the x and y profiles which are reasonable approximation of the engineering surfaces (15).

Since the engineering surfaces exhibit directional properties due to manufacturing processes and/or running-in, these properties of the surfaces are projected by γ , surface pattern parameter, which is the ratio of x and y correlation lengths.

It is observed that shear and pressure flow factors are strongly dependent on the exact topography of the surface. The values may differ considerably even though they are evaluated for statistically identical surfaces. The scatter in these values tends to increase as h/σ becomes less than 3. This is mainly due to increased dependence of flow factors on h/σ and the directional properties of the roughness. Some typical examples of scattering are given in Table 1. Since it is found that the flow factors do vary, we decided to evaluate the flow factors for several different but statistically identical surfaces and average them. The values presented in this thesis are the average of 20 runs, which are believed to give meaningful averages.

When h/σ becomes less than 3 the asperities start interacting. This regime is called partial lubrication regime. Many bearings encountered in practice operate in this regime. Given the importance of partial lubrications, it is decided to consider only the cases where $h/\sigma < 3$. However, when h/σ is less than .5 the asperity contact may become so severe that it forms barriers, and allows no flow through the bearing. This behaviour of the contact may result in unrealistic values for the flow factors. Therefore, for the above range of the values of h/σ, the use of this model is not advised.

Pressure Flow Factor

The pressure flow factors presented in this sectin are obtained using the model problem 1 described in Appendix A. They are usually an average of twenty runs which use different but statistically identical surfaces as indicated in the previous section. It is evident that ϕ_x is not a function of velocity since it does not appear in the formulation of model problem 1, and it is also not a function of the nominal pressure gradient due to the fact that ϕ_x is normalized by this quantity (Eq. A-16). The pressure flow factor is then only a function of the film thickness — standard deviation of roughness ratio and surface pattern parameter of the combined roughnes, that is,

$$\phi_x = \phi_x(h/\sigma,\gamma)$$

In Patir and Cheng's work (14), a no flow boundary condition is used for the sides of the element. This boundary condition is justified if the elements used in the average Reynolds Equation contain a large number of asperities. However, it is of interest to determine the effect of an open type side boundary, as shown in Figure 21, on the pressure as well as shear flow factors.

The results in this section are designed primarily to examine the difference between the closed and open boundary conditions. They are presented as functions of h/σ and γ . In addition, the effect of the ratio of the element length to asperity length is studied.

In Figure 20, ϕ_x values are plotted against the h/σ for $\gamma = 1$. The solid line in the figure represents the average values, while the dotted lines show the minimum and maximum deviation from the mean. As it is also evident from the figure that the scatter in these values increases as h/σ decreases, this is mainly due to the fact that a small deviation from isotropy results in a large change in ϕ_x . Therefore, the flow factors obtained from different surfaces scatter.

Figure 21 shows the average pressure flow factor values with open side boundary for isotropic, transverse and longitudinal roughness. For surfaces having larger correlation lengths in the longitudinal direction ($\gamma > 1$), the pressure flow is enhanced. Therefore, ϕ_x is greater than unity, but for isotropic and transverse roughness, ϕ_x is smaller than one and shows a decreasing trend when h/σ decreases from 3 to about 1. For $h/\sigma < 1$,, an uptrend for ϕ_x is evidenced.

Figure 22 shows a comparison of ϕ_x between the open boundary solution and the closed boundary solution. It is seen that the open boundary solution yields a higher value of ϕ_x particularly for low values of h/σ. This discrepancy seems to pose a question on whether the close boundary solution is a good approximation for calculation of these flow factors. This question was resolved by some additional runs on the effect of N/λ_x on the pressure flow factor ϕ_x . The ratio N/λ_x represents approximately the number of asperities in the simulated region. It shows very clearly that the open boundary solutions are affected by the value of N/λ_x whereas the close boundary solution is totally insensitive to any change of N/λ_x . As N/λ_x becomes large, the two solutions appear to converge. This result suggests that the closed boundary solution is indeed a good approximation for calculation of flow factors as long as there are 10-15 or more asperities within the elemental area for which ϕ_x or ϕ_s will be used. Recently Tondor (16) and also Teale and Lebeck (17) also used an approach similar to Patir and Cheng's to calculate pressure flow factors for isotropic.

Tondor obtained values of the pressure flow factors surfaces much higher than those calculated by Patir and Cheng. Tondor's model corresponding to the open boundary solution but with only one or two asperities in the region of simulation. The results shown in Figure 23 explains that the over estimate of ϕ_x from Tondor's model is mainly due to the small sample of asperities in the simulated region. It is believed that for the average flow model to be meaningful there must be sufficient asperities in the simulated region to account for the integrated effect. For this reason, it appears that the close boundary solution should be the most meaningful results for the average flow model Reynolds equation.

Shear Flow Factor

The shear flow factors obtained using the open-boundary model are presented here. The values are computed for twenty surfaces and then averaged. Similar to the pressure flow factor, the shear flow factor is also a function of film thickness and the roughness parameters alone. However, unlike ϕ_x which only depends on the statistics of the combined roughness, the shear flow factor depends on the statistical parameters of rouoghness of both surfaces separately. If we consider a bearing in which surface 1 is moving and surface 2 stationary, and if the two surfaces are statistically identical, there will be no net flow due to the combined effect of sliding and roughness. If the rough surface is moving, the fluid carried in the valleys will result in an additional flow transport, and yield a positive ϕ_s. On the other hand, if the smooth surface is moving, the fluid, trapped in the valleys of the rough surface, will reduce the flow and produce a negative ϕ_s. Although the shear flow factor depends on the surface roughness parameter of both surfaces, since, in this study, the values are obtained by using a smooth surface and a set of statistically identical surfaces, this dependence is not cosidered as a parameter.

In Figure 24, ϕ_s is plotted against the nominal film thickness for different surface pattern parameters. As expected, ϕ_s approaches zero as h/σ increases because of the vanishing effect of roughness; however, the flow transport due to the roughness reaches a maximum somewhere around $h/\sigma = 1$, and then drops rapidly towards zero. This behaviour is related to the contacts at partial lubrication regime. Since contacts do not permit flow, σ_s is decreased due to the decrease in available flow areas as h/σ drops below 1.

Since the longitudinal roughness allows flow between valleys the flow transported by the valleys of the roughness for the longitudinal roughness is less than that transported by the transverse roughness. The ϕ_s curves for the transverse roughness are at a much higher level than the ϕ_s curves for either isotropic or longitudinal roughness. The use of an open boundary on the sides produces shear flow factors slightly lower than those obtained with a closed boundary condition (Fig. 25). As seen in Figure 26, the open boundary solution is sensitive to the average number of asperities with the simulated region, N/λ_x . As this number increases, there is hardly any difference between the open and closed boundary solutions.

IX SUMMARY

Work initiated in understanding the cavitation phenomenon in a narrow gap between sealing surfaces has led to the following results:

a) An experimental rig consisting of a hydrostatic circular step pad was constructed to simulate the cavitation phenomenon under a water pressure up to 2000 psi comparable to those in the submarine stern-tube seals. Cavitation bubbles were observed for water glycerine, and their mixtures.

b) Several analytical models were studied, and the physical parameters influencing bubble growth and collapse were identified. An analysis was also made to determine the axisymmetric stress in the solid induced by a sudden pressure distribution during the collapsing of a bubble.

c) An existing thin-film analysis for determining the flow factors used in the hydrodynamic analysis of rough surfaces was extended to include the steady-state cavitation effects. Results showed that

1) The shear flow factors ϕ_s^* calculated using a model considering cavitation (Model 3 in Appendix A) are found to be dependent on ambient pressure P_a as well as surface pattern parameter γ and the film thickness to roughness ratio, h/σ. The ϕ_s^* increase as P_a increases, and otherwise, exhibits the same behaviour as the non-cavitated model with respect to changes in h/σ and γ.

2) The model predicts a lower shear flow factor when cavitation is considered. They approach asymptotically to the non-cavitated values as the ambient pressure rises.

3) The effect of cavitation are found to be less significant for $h/\sigma > 3$ or for $h/\sigma > 0.75$ and more significant for the intermediate values.

4) The surfaces with transverse roughness resulted in more cavitated regions than isotropic and longitudinal roughness.

REFERENCES

1. Winn, L. W., and McCormick, J. "Trident Main Shaft Seal Analysis," Mechnical Technology Inc. Technical Report MTI 76 TR51, Sept. 1976.

2. Hueter, T. F., and Bolt, R. M. Sonics, John Wiley and Son, New York, p. 220, 1955.

3. Knapp, R. T., Daily, J. T., and Hammitt, F. G. "Cavitation, McGraw-Hill, New York, pp. 321-361, 1970.

4. Ibid. p. 169.

5. Ibid. pp. 160-161.

6. Cameron, A. Basic Lubrication Theory, Halsted Press, New York, p. 26, 1976.

7. Knapp, op. cit. p. 104.

8. Bretherton, F. P. "The Motion of Long Bubbles in Tubes," J. Fluid Mechanics, 10, pp. 166-188, 1961.

9. Taylor, G. I. "Cavitation of a Viscous Fluid in Narrow Passages," J. Fluid Mechanics, 16, pp. 595-619, 1963.

10. Knapp, op. cit. p. 335.

11. Timoshenko, S. P., and Goodier, J. N. Theory of Elasticity, McGraw-Hill, New York, p. 405, 1970.

12. Burton, R. A. "Effects of Two Dimensional, Sinusoidal Roughness on the Load Support Characteristics of a Lubricant Film," Trans. ASME, D85, p. 258, 199963.

13. Hamilton, B. D., Walowit, J. A., Allen, C. M. "A Theory of Lubrication by Microirregularities," J. of Basic Engineering, March 1966/177.

14. Patir, N., and Cheng, H. S. "An Average Flow Model for Determining Effects of Three Dimensional Roughness on Partial Hydrodynamic Lubrication," J. of Lubrication Technology, Vol. 100, No. 1, January 1978.

15. Patir, N. "Numerical Procedure for Random Generation of Rough Surfaces," WEAR, Vol. 47, No. 2, p. 258, 1978.

16. Tondor, K. "Simulation of the Lubrication of Isotropically Rough Surfaces," ASLE Trans. 23, July 1980.

17. Teale, J. L., and Lebeck, A. O. "An Evaluation of the Average Flow Model for Surface Roughness Effects in Lubricaton," ASME/ASLE Lubrication Conference, Paper 79-Lub-37, 1979.

TABLE 1

SCATTER IN ϕ_x VALUES

h/σ	$\lambda_x = \lambda_y$	M=N	γ	ϕ_x max	ϕ_x average	ϕ_x min
.75	3	25	1	.99253	.90403	.85333
1	3	25	1	1.03306	.85140	.73472
1.5	3	25	1	1.11279	.83785	.62215
2	3	25	1	1.36528	.90924	.53607
3	3	25	1	1.71792	1.07882	.36928

BUBBLE DYNAMICS
LIMITING CASES

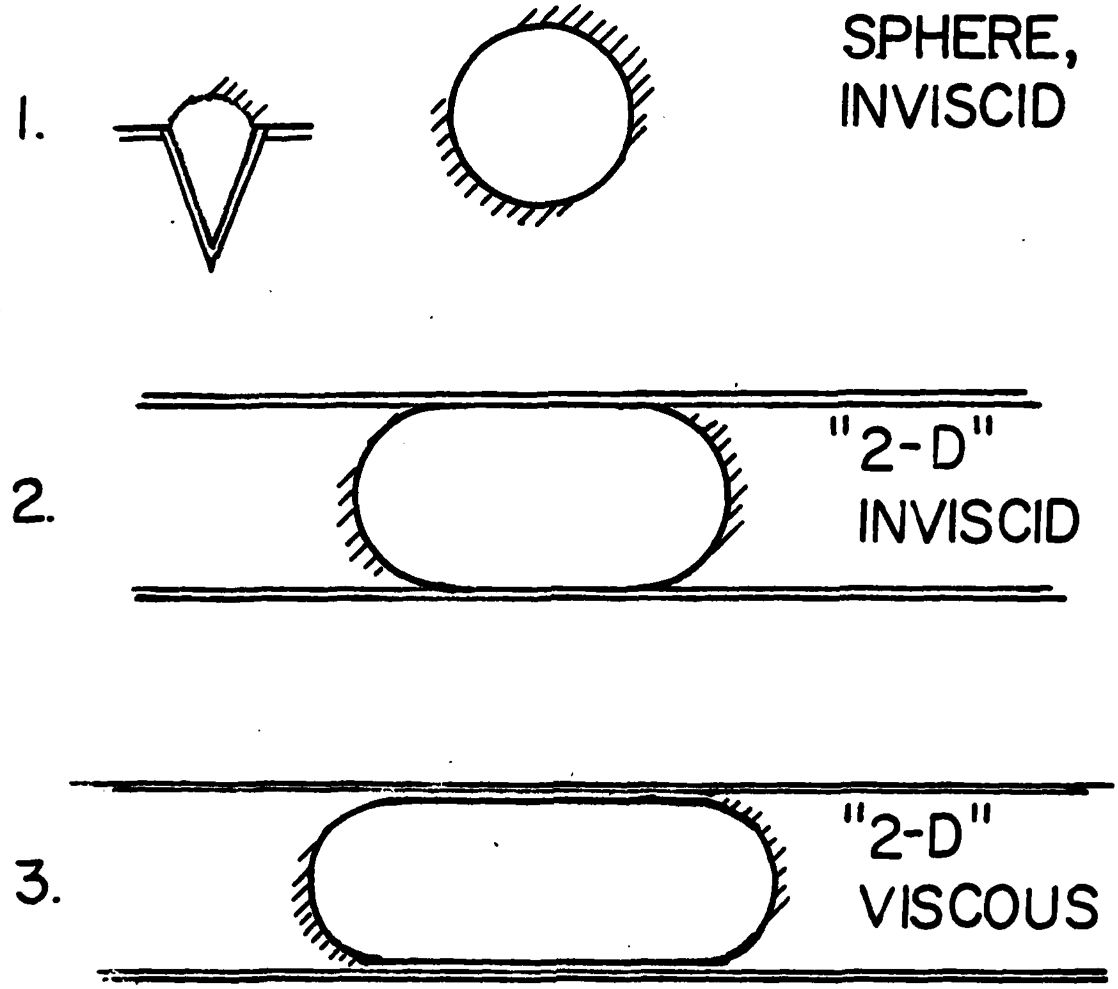

Figure 1. Possible bubble shapes in the liquid.

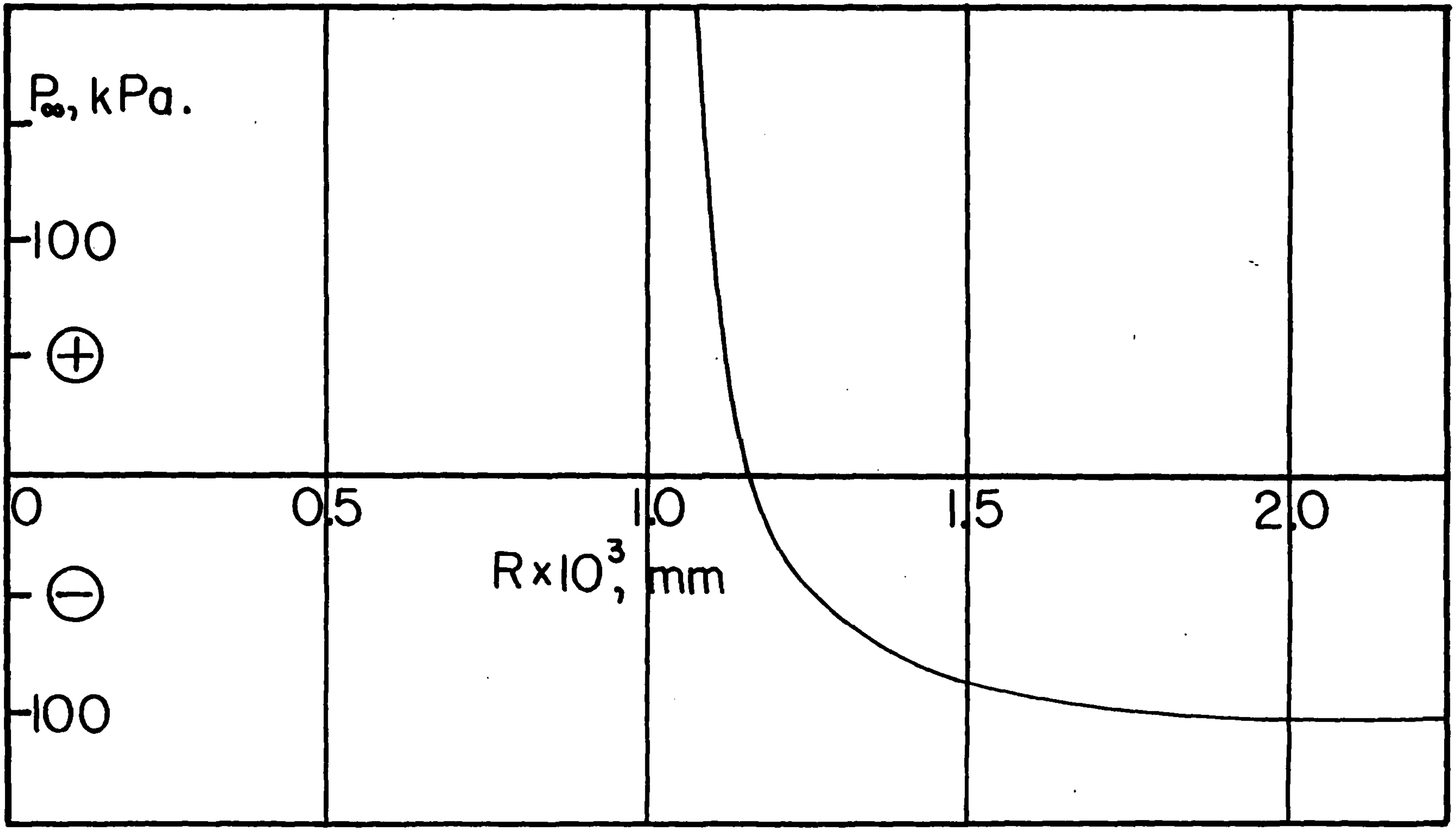

Fig. 2. Equilibrium bubble radius for different ambient pressures. The fluid is water. σ = 0.0733 N/M, p_r = 2.5 KPa, η = 1.25 μ.

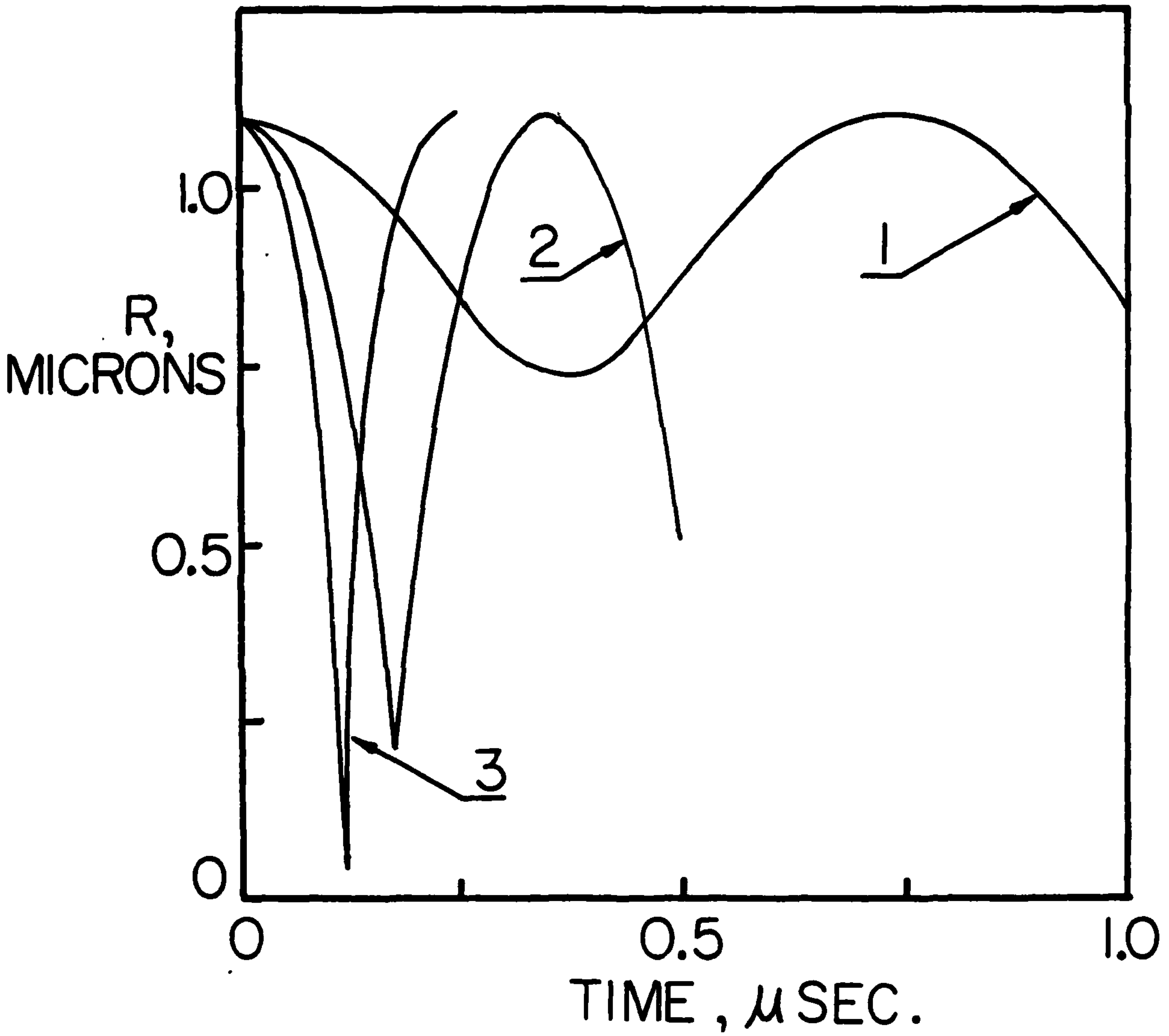

Fig. 3. Bubble response to a step increase in pressure. Initial $R = 1.1\,\mu$, $\eta = 1.25\,\mu$. Fluid is water. Each curve corresponds to a different pressure increment. 1.$\Delta p = 0.1$ MPa; $\Delta p = 0.5$ MPa; 3.$\Delta p = 1.0$ MPa.

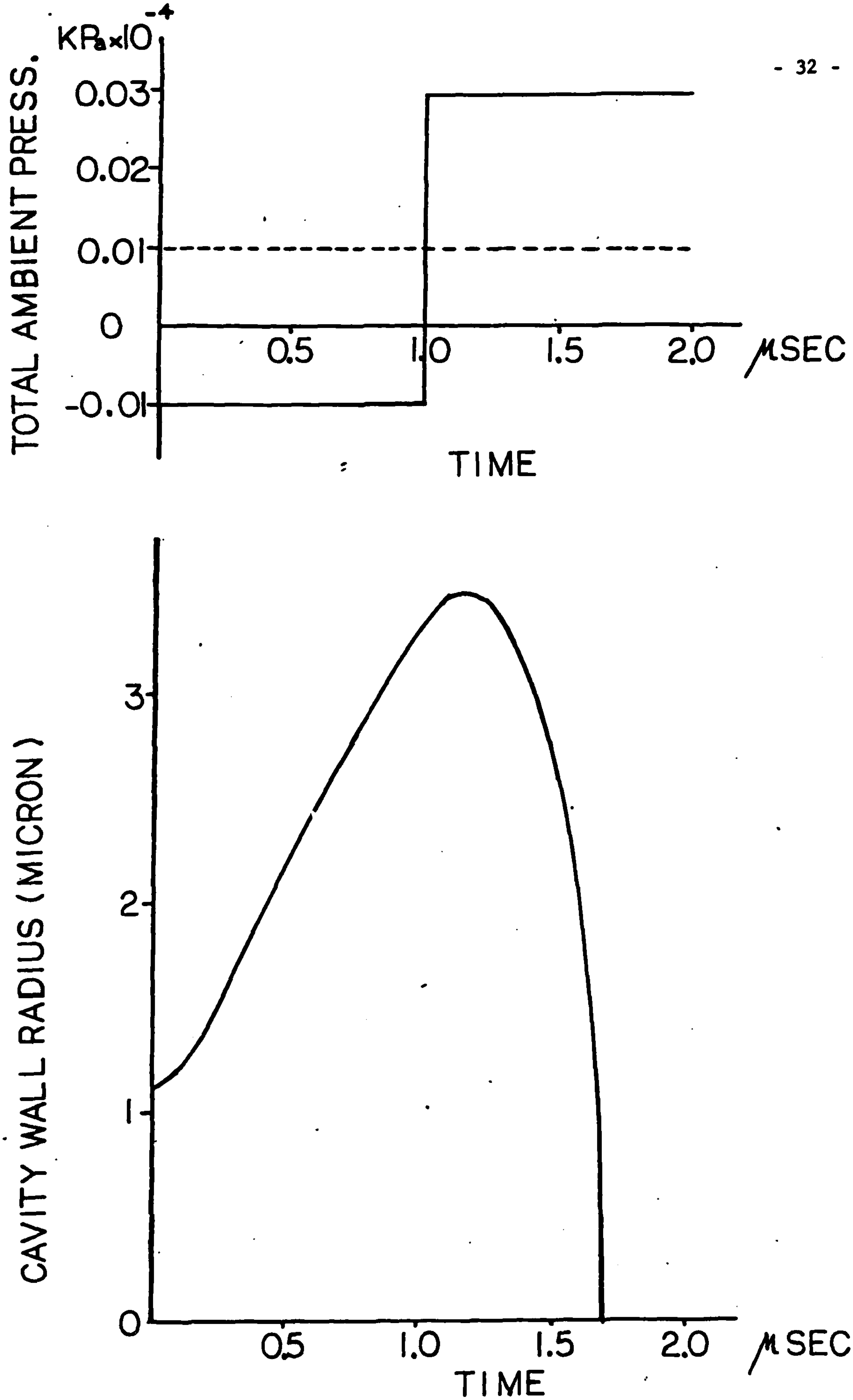

Figure 4. Bubble response to first a pressure decrease and then a pressure increase. Bubble data are the same as in Fig. 3.

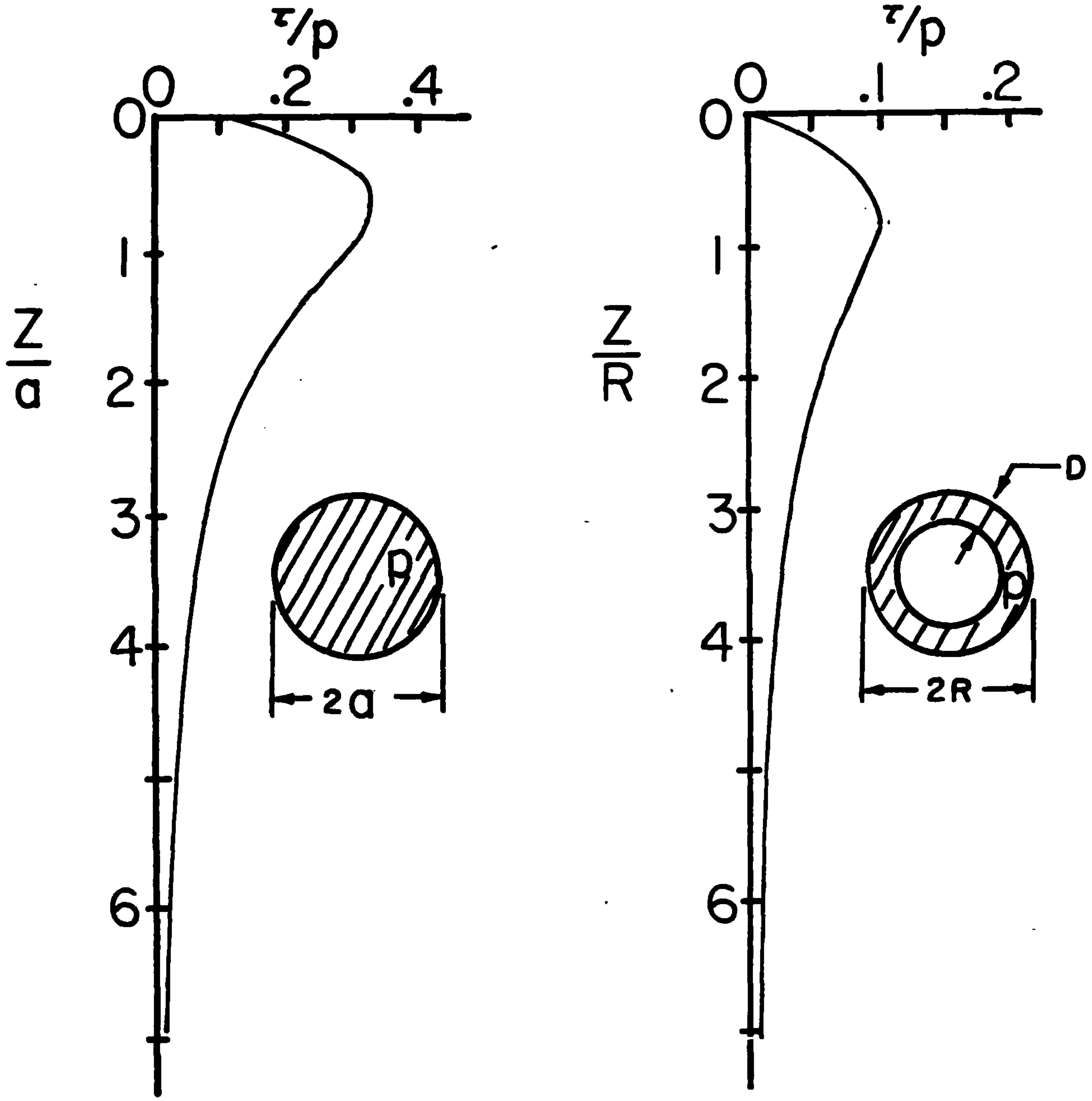

Fig. 5. Shear stress distribution in a solid beneath a region on its surface with an applied axi-symmetric pressure distribution. The shear on the axis is shown. The surface is at Z = 0. The shaded areas show the shape of the pressure distribution on the surface.

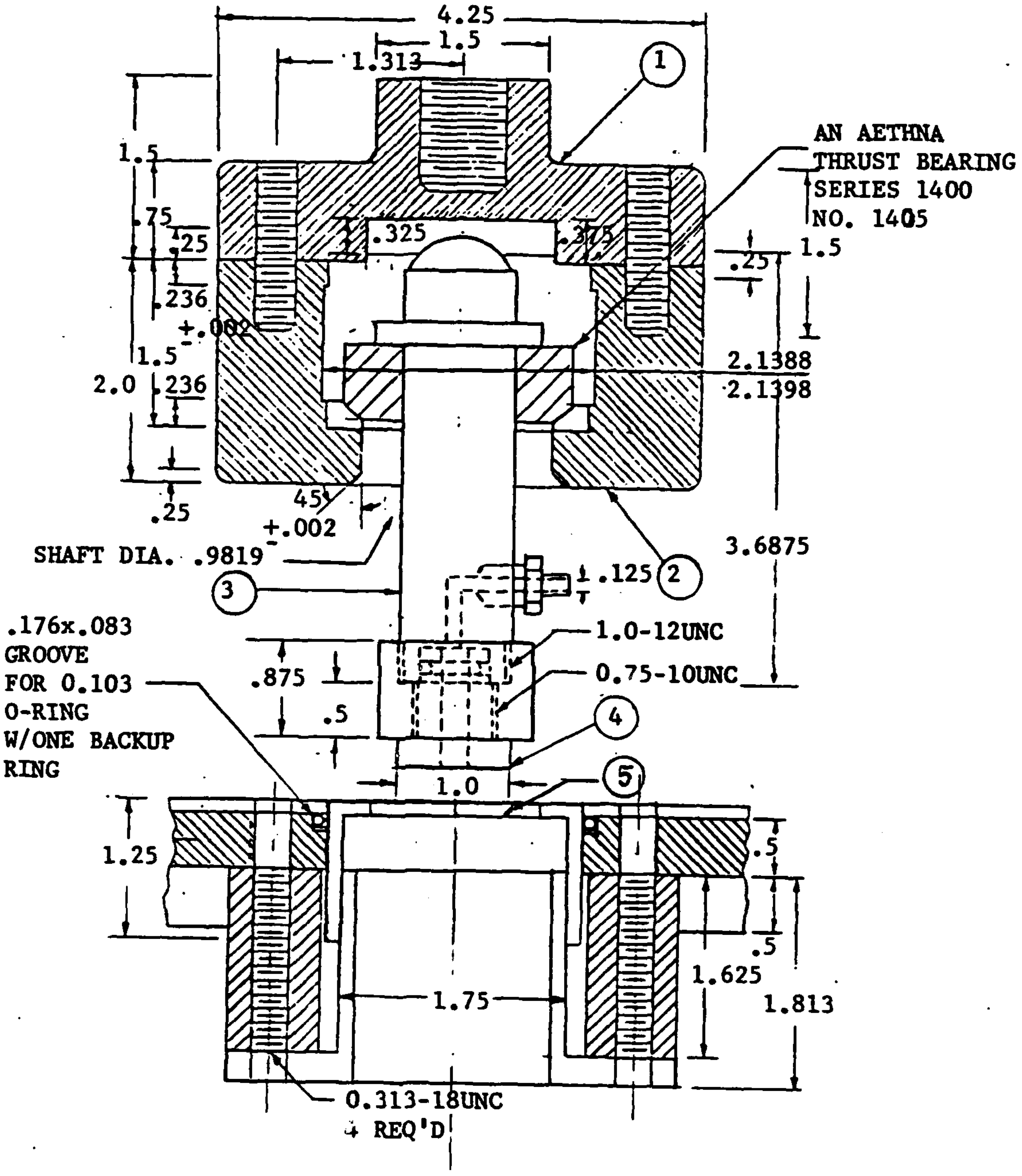

Fig. 6. Drawing of the test region of the cavitation apparatus. Dimensions are in inches. 4 is the test surface. 5 is the quartz surface mounted on the load cell.

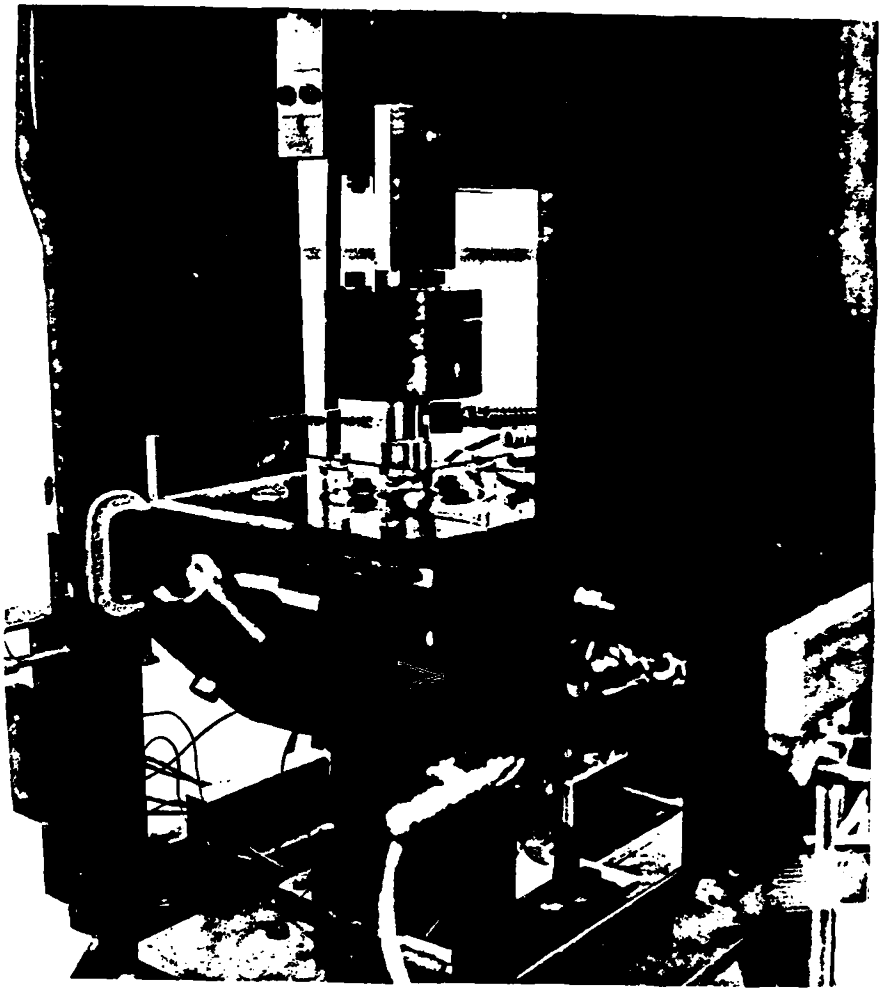

Figure 7. The test area of the experimental apparatus.

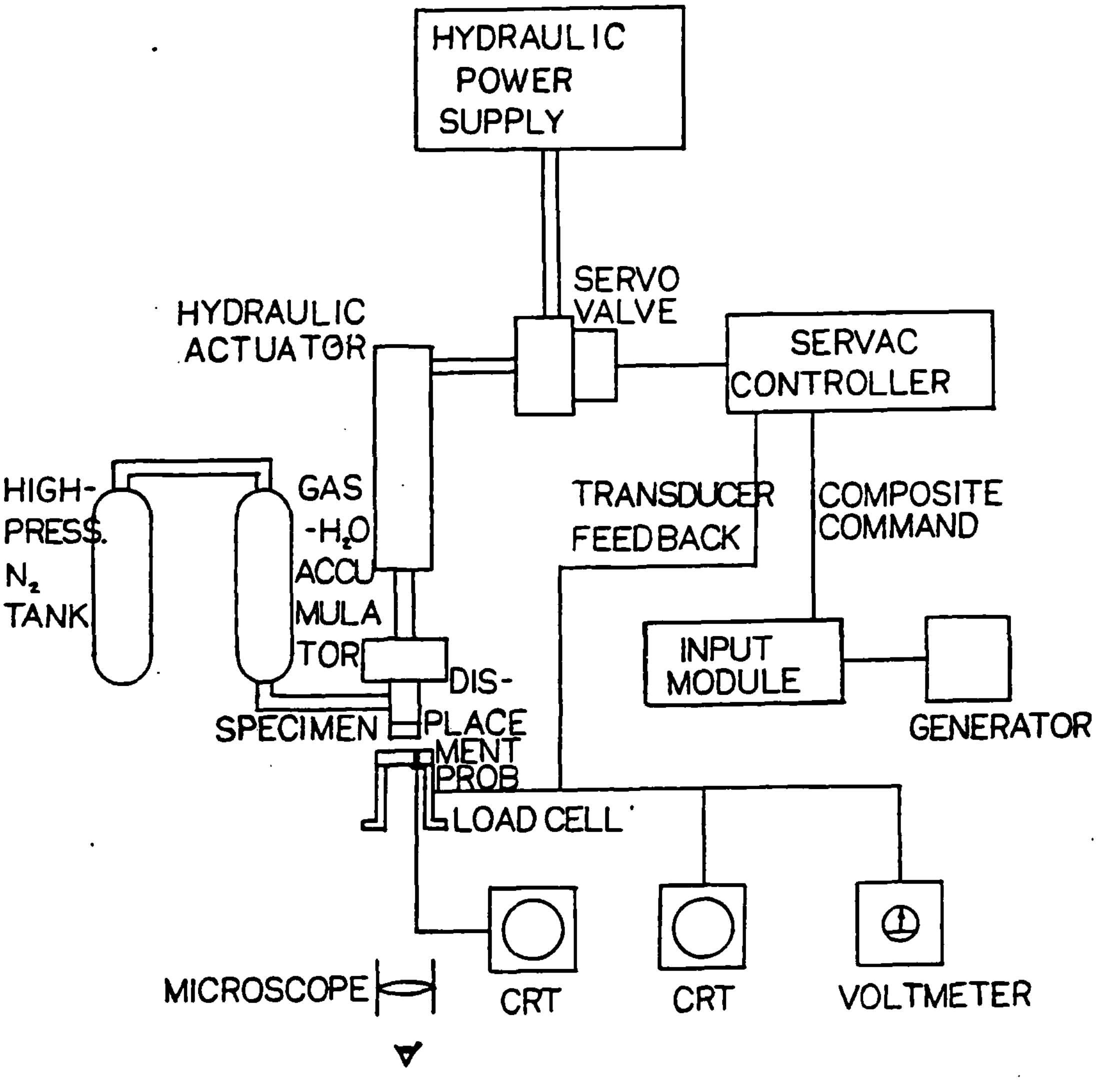

Fig. 8. The drive and instrumentation system for the cavitation apparatus.

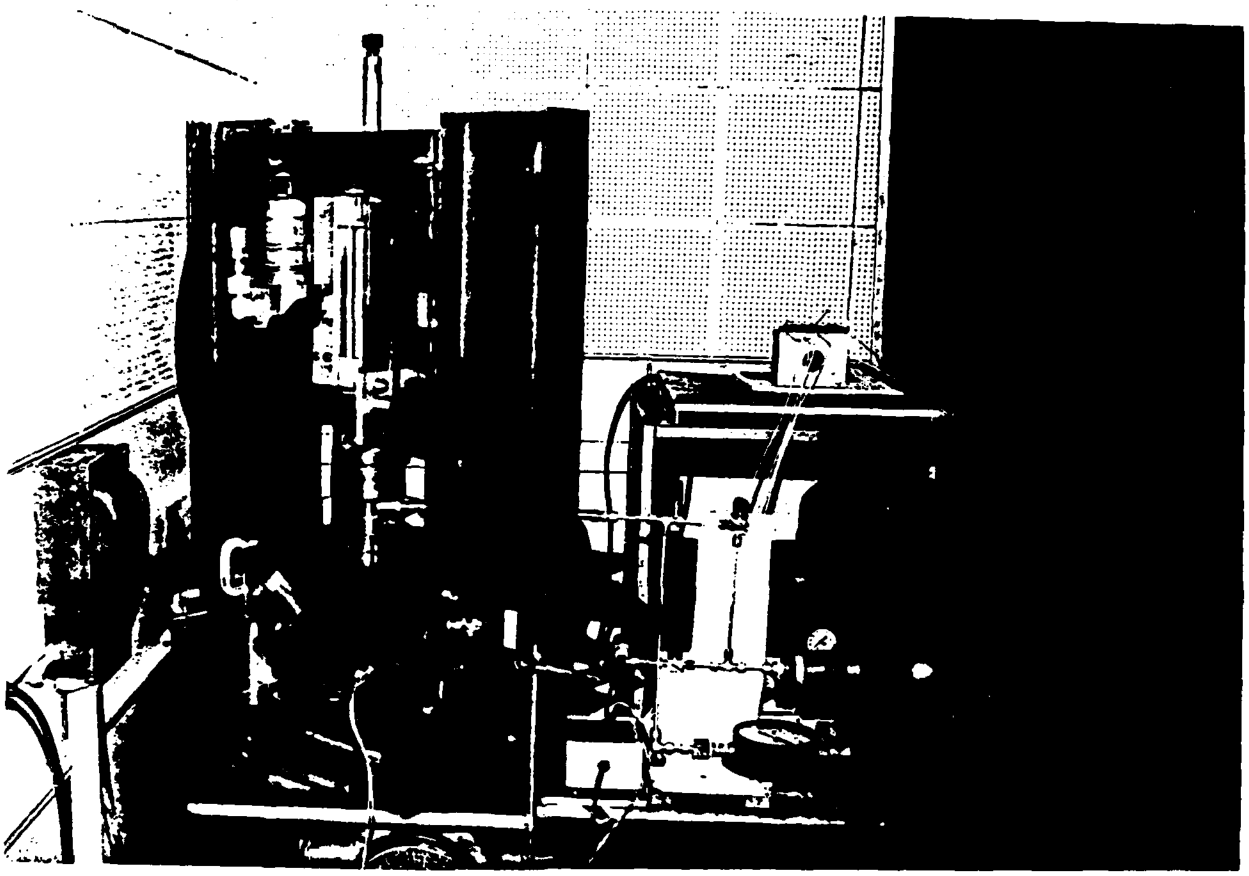

Figure 9. A general view of the experimental apparatus. The hydraulic accumulator is to the right, the hydraulic power supply is in the background, and the test region is to the left.

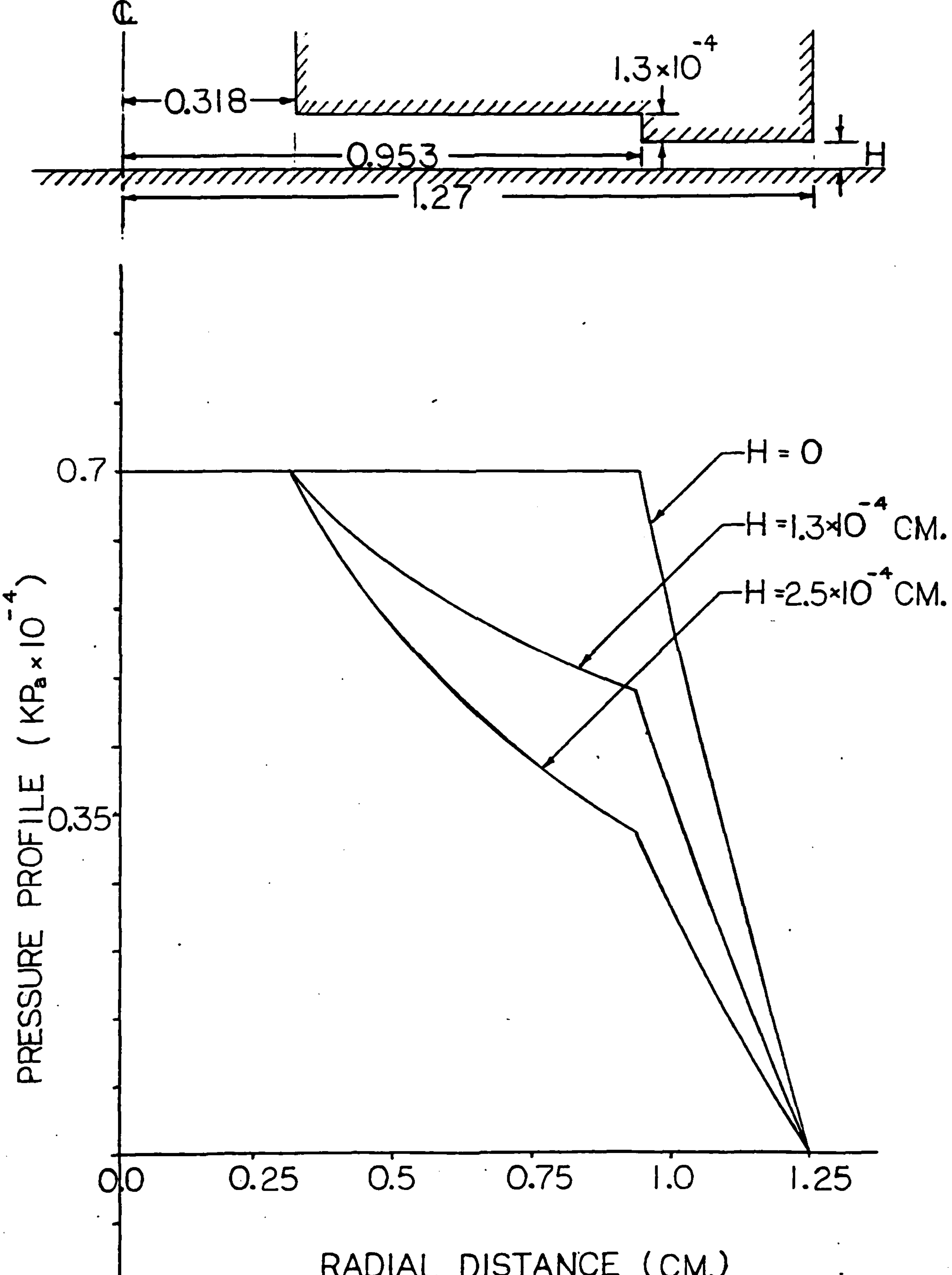

Fig. 10. Static pressure distribution for a stepped test surface. The total force on the test surface depends on the gap.

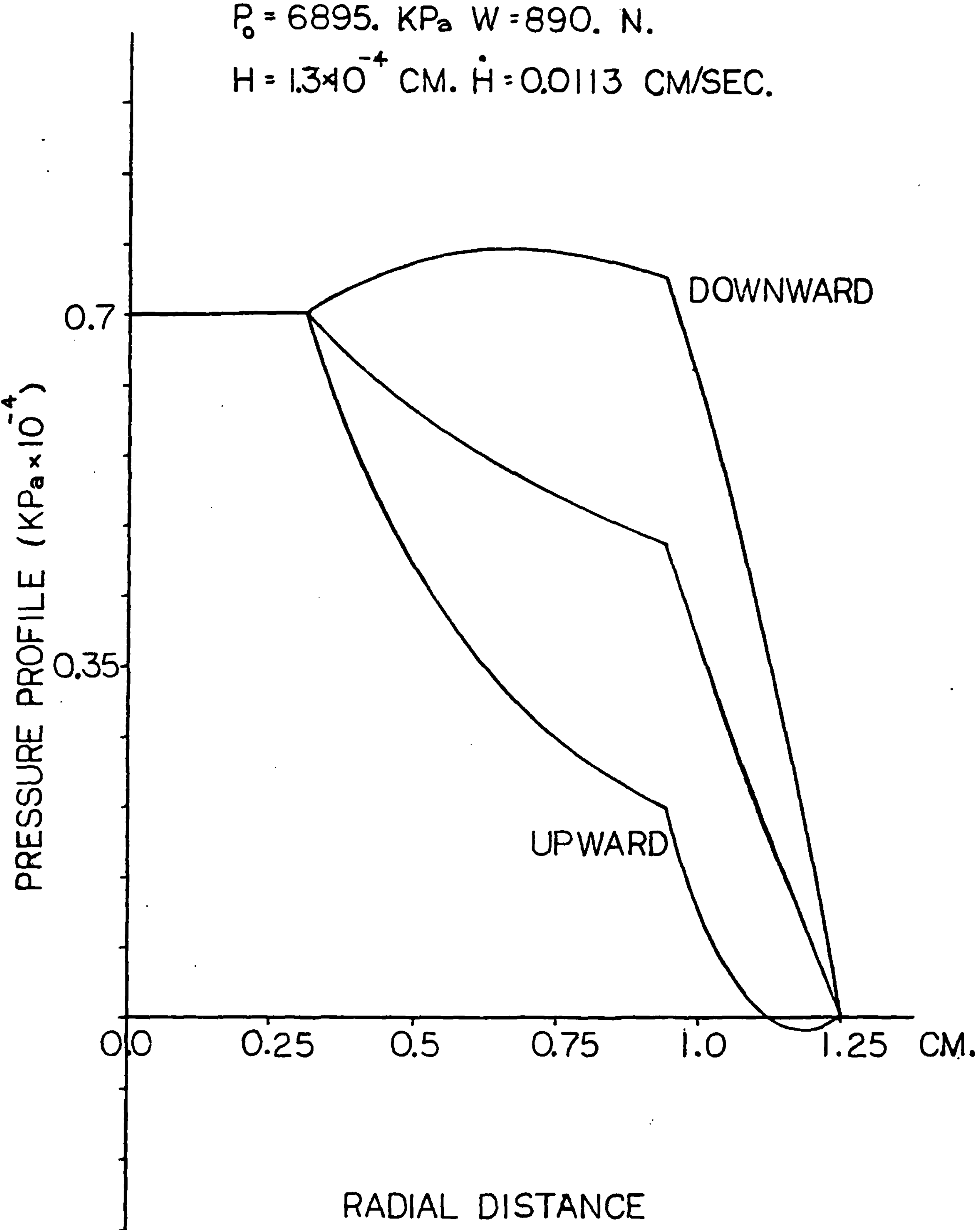

Fig. 11. Variation of the pressure distribution with velocity for the stepped surface. $\dot{H}$ is the gap height velocity

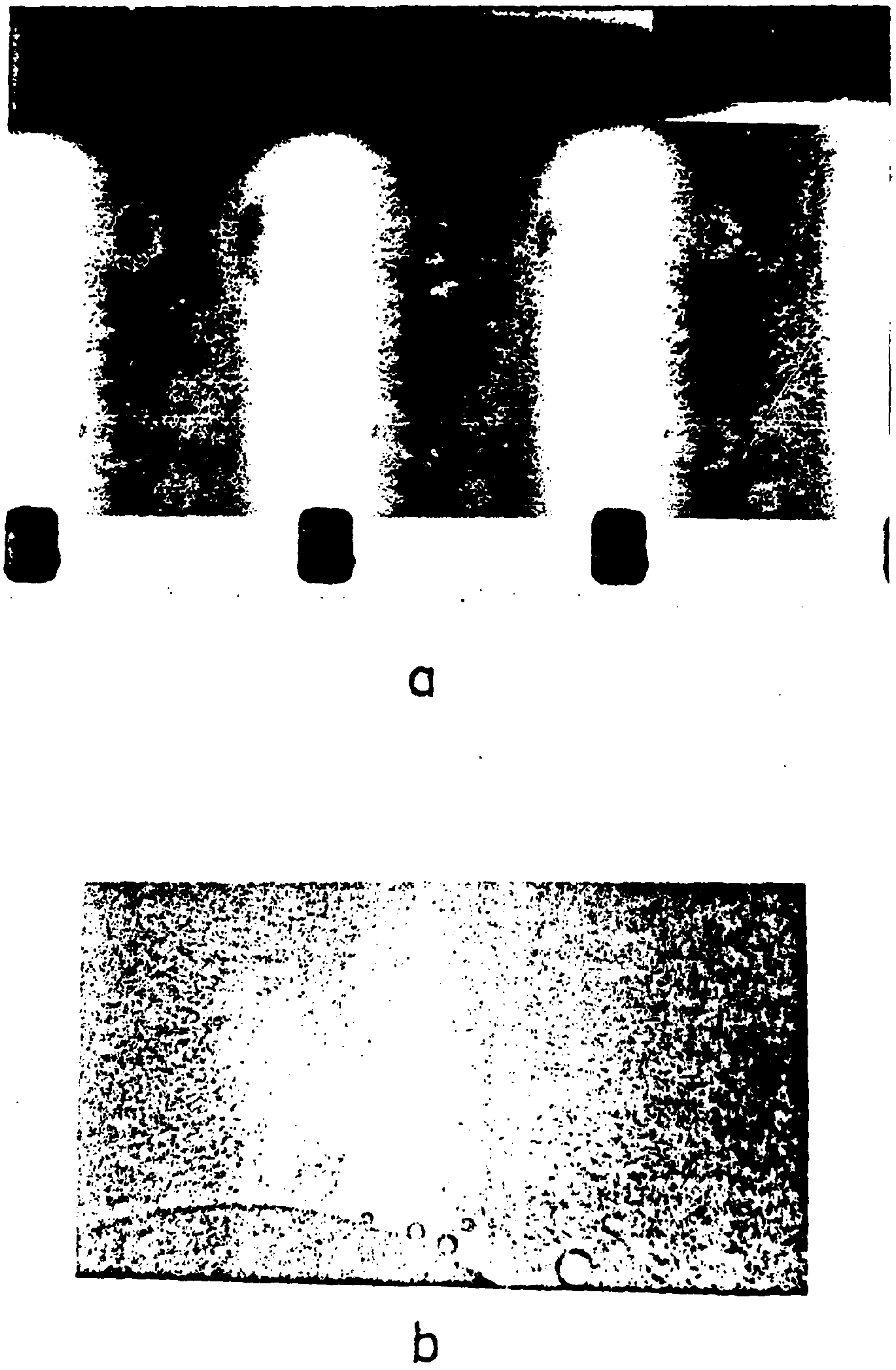

Fig. 12. Micrographs of bubbles appearing in the gap when the gap height changes with time. a) shows a time sequence at 1000 frames/sec of bubbles in a water-glycerin solution; b) shows bubbles in pure water.

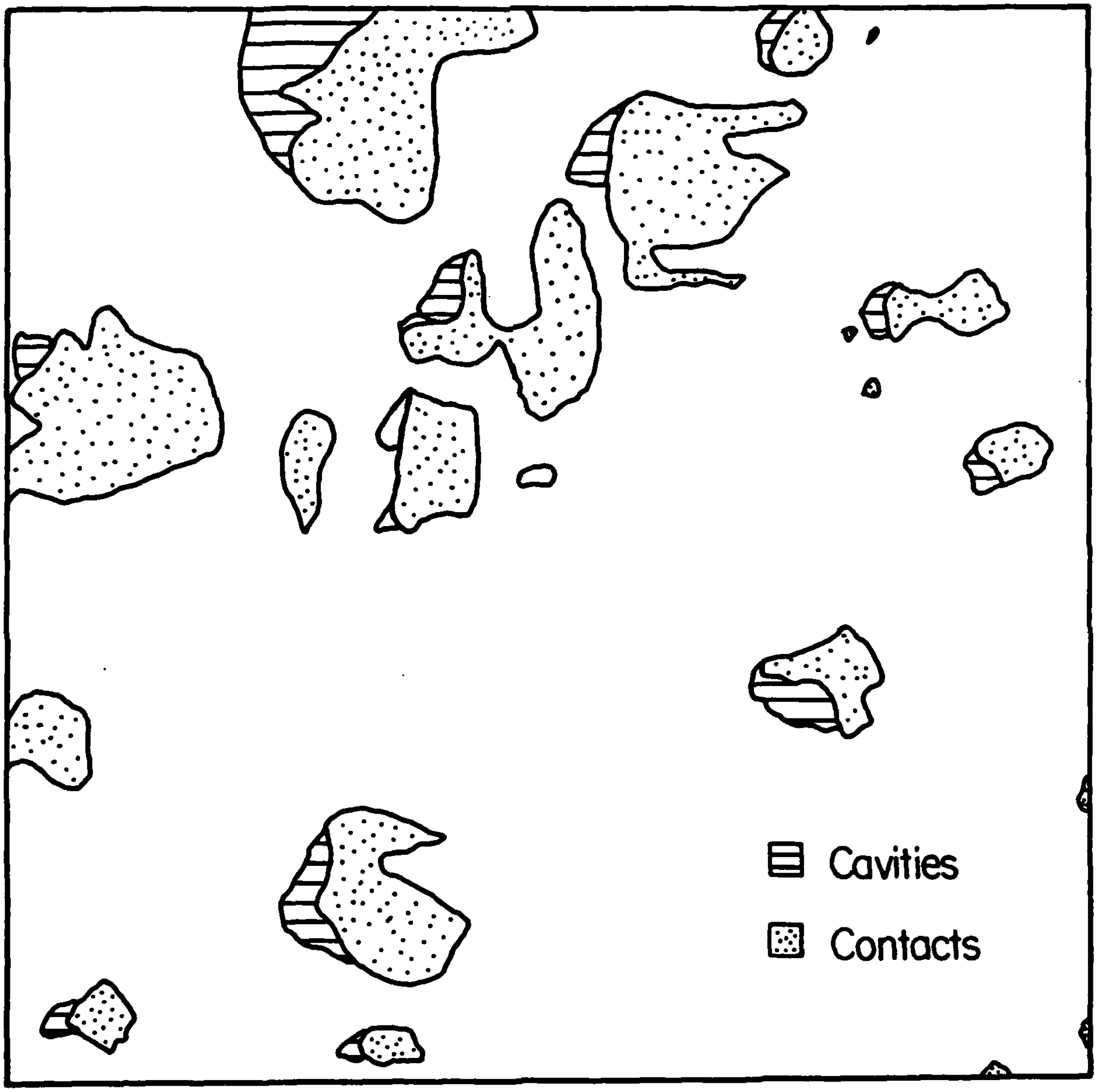

Figure 13

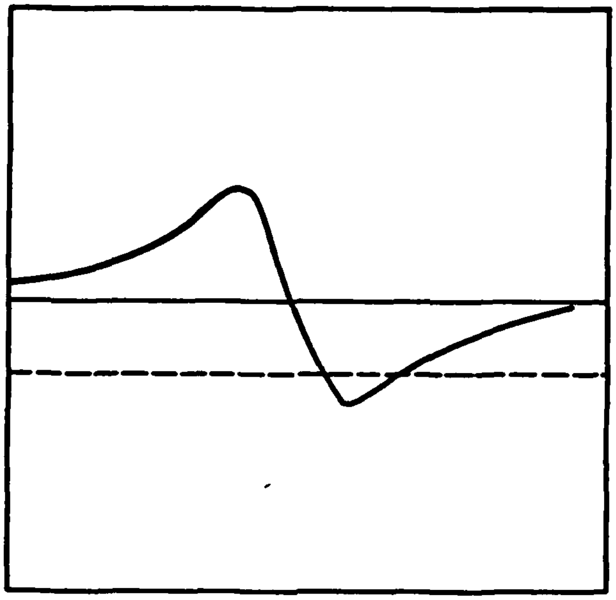

No Cavitation

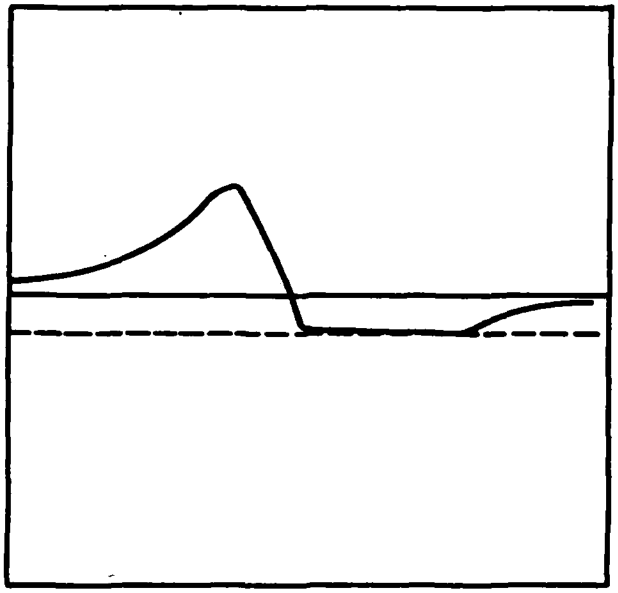

Cavitation Occurs

Figure 14. Pressure distribution about an asperity.

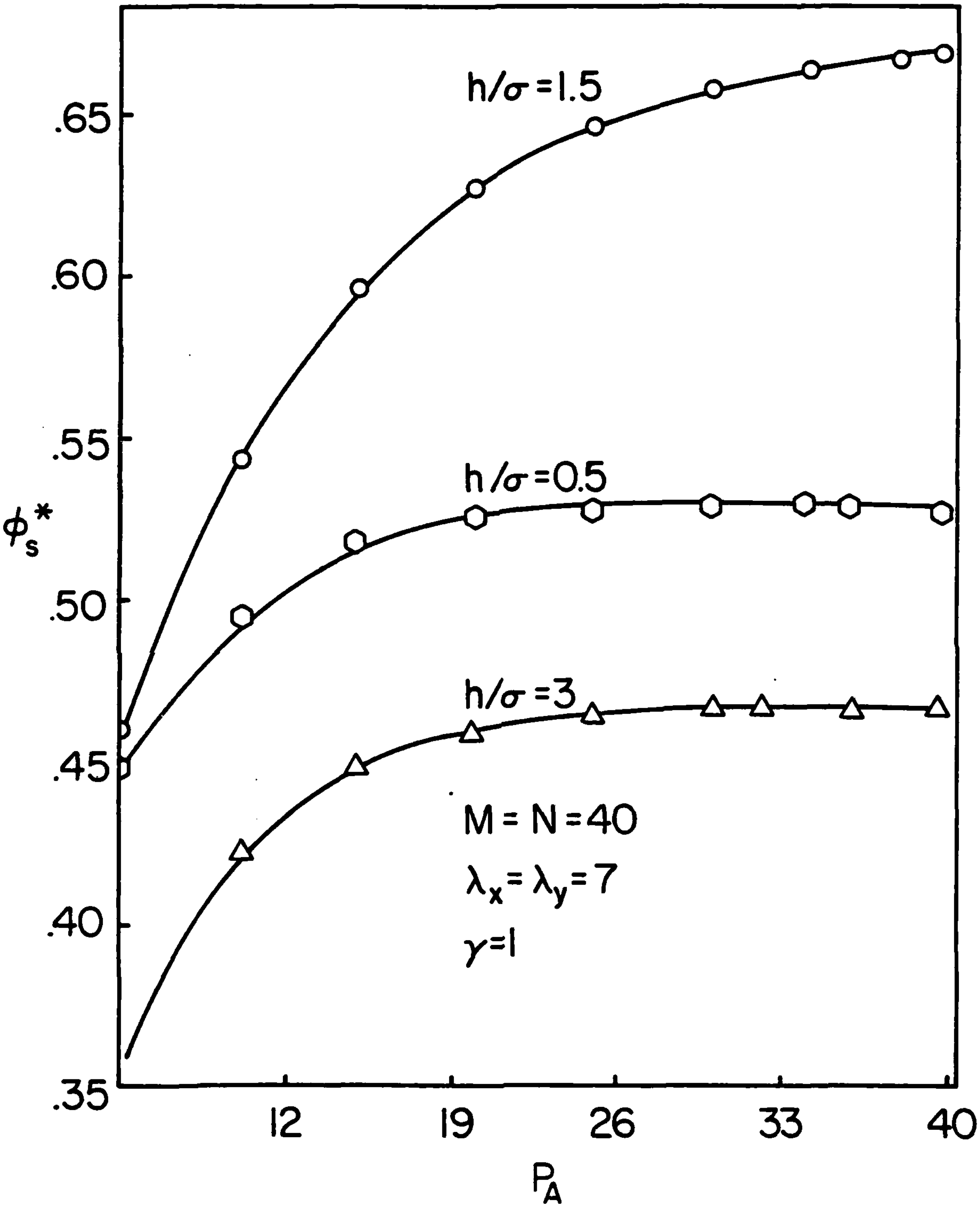

Figure 15. Shear flow factor for isotropic surfaces.

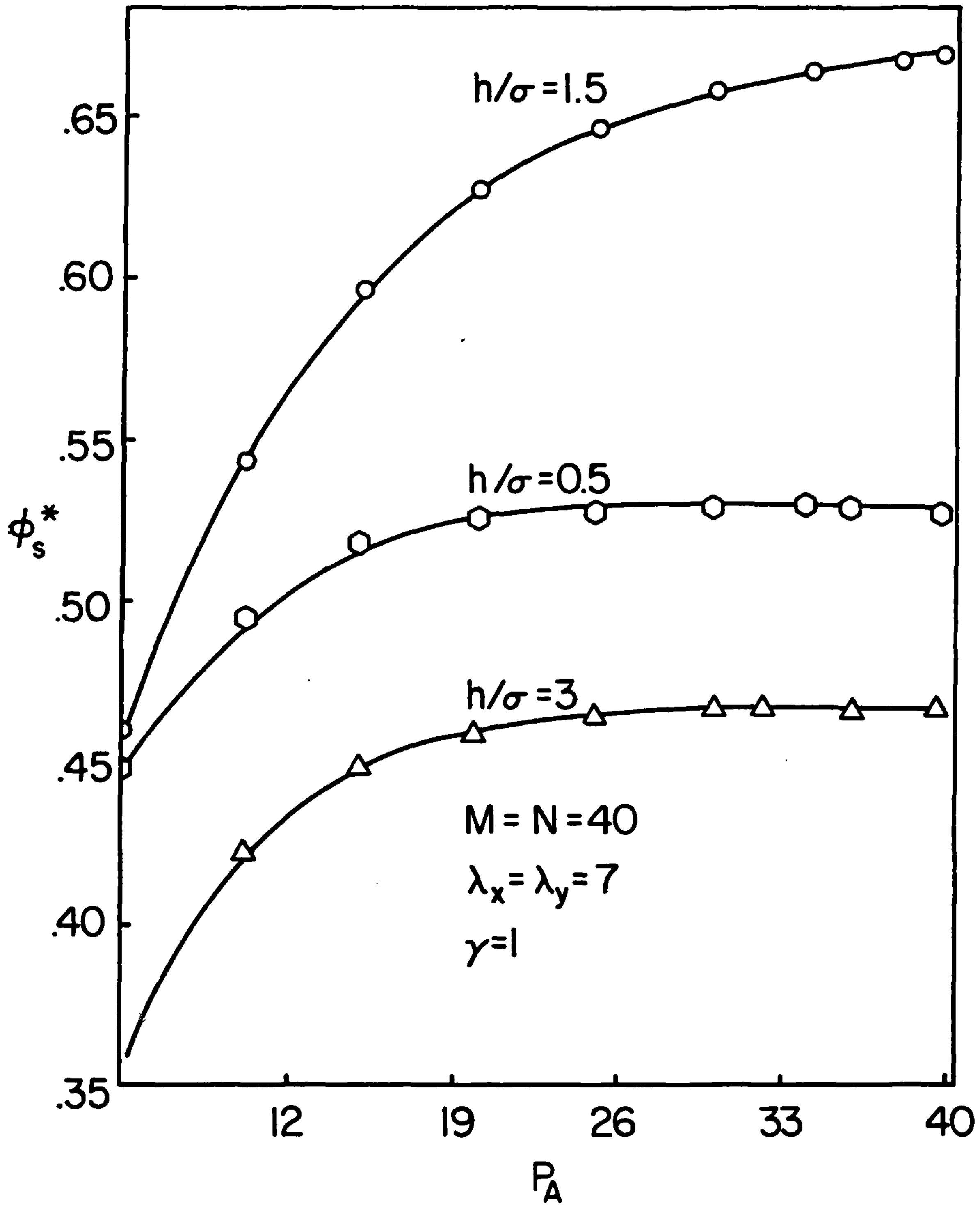

Figure 16. Change of shear flow factor by ambient pressure for isotropic, transverse and longitudinal surfaces.

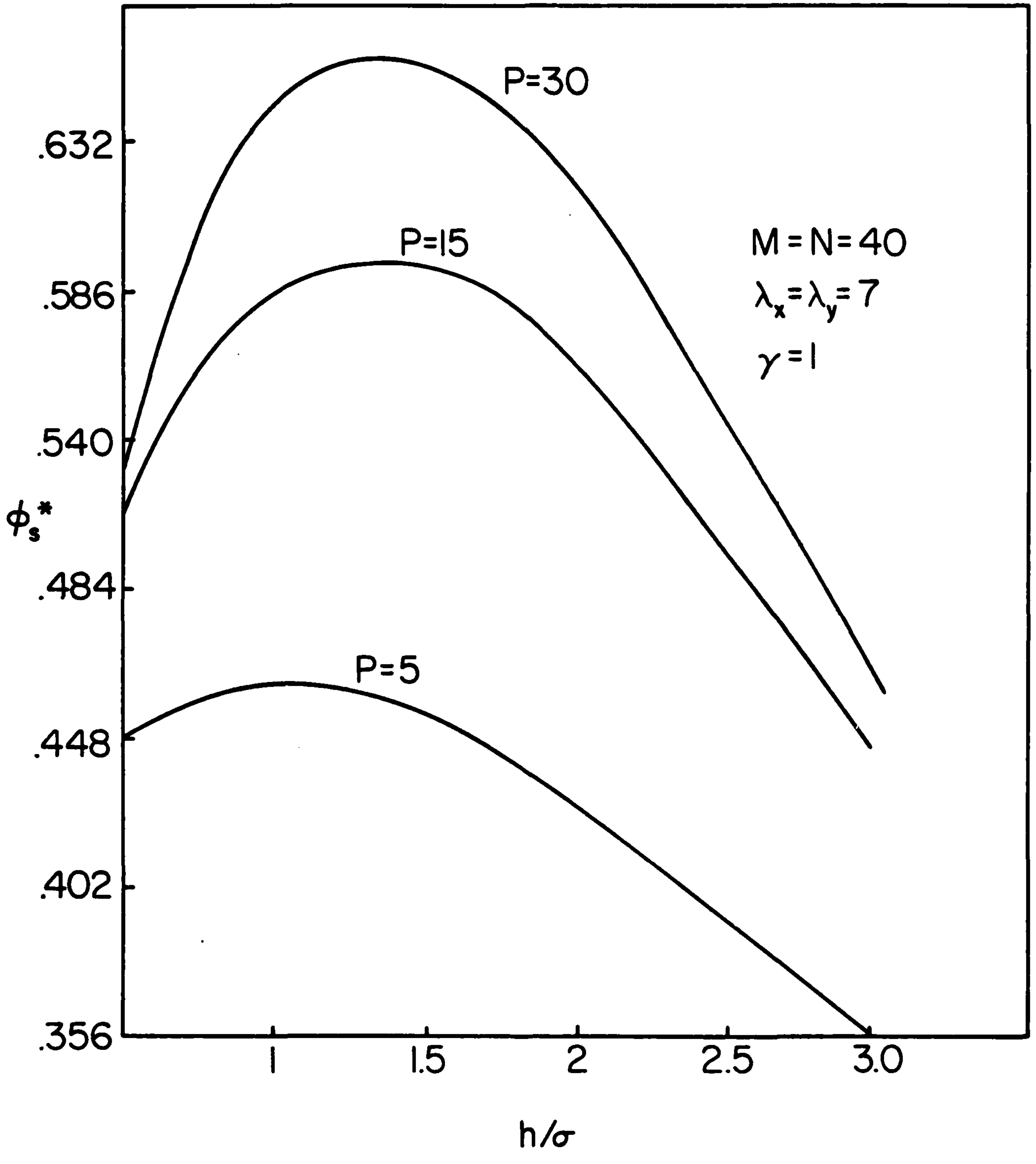

Figure 17. Change of shear flow factor with h/σ for different ambient pressures.

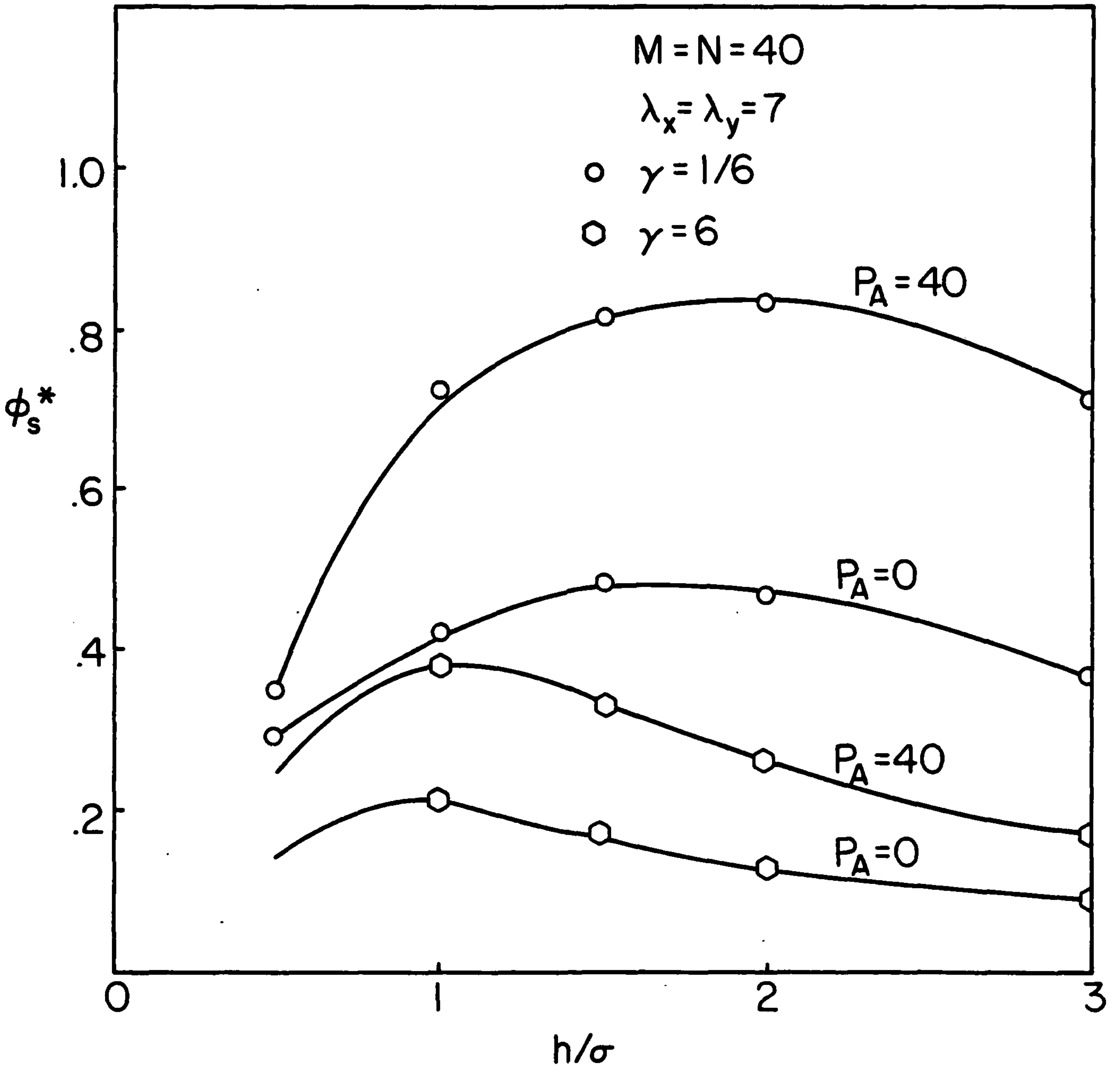

Figure 18. Shear flow factor for transverse and longitudinal surfaces.

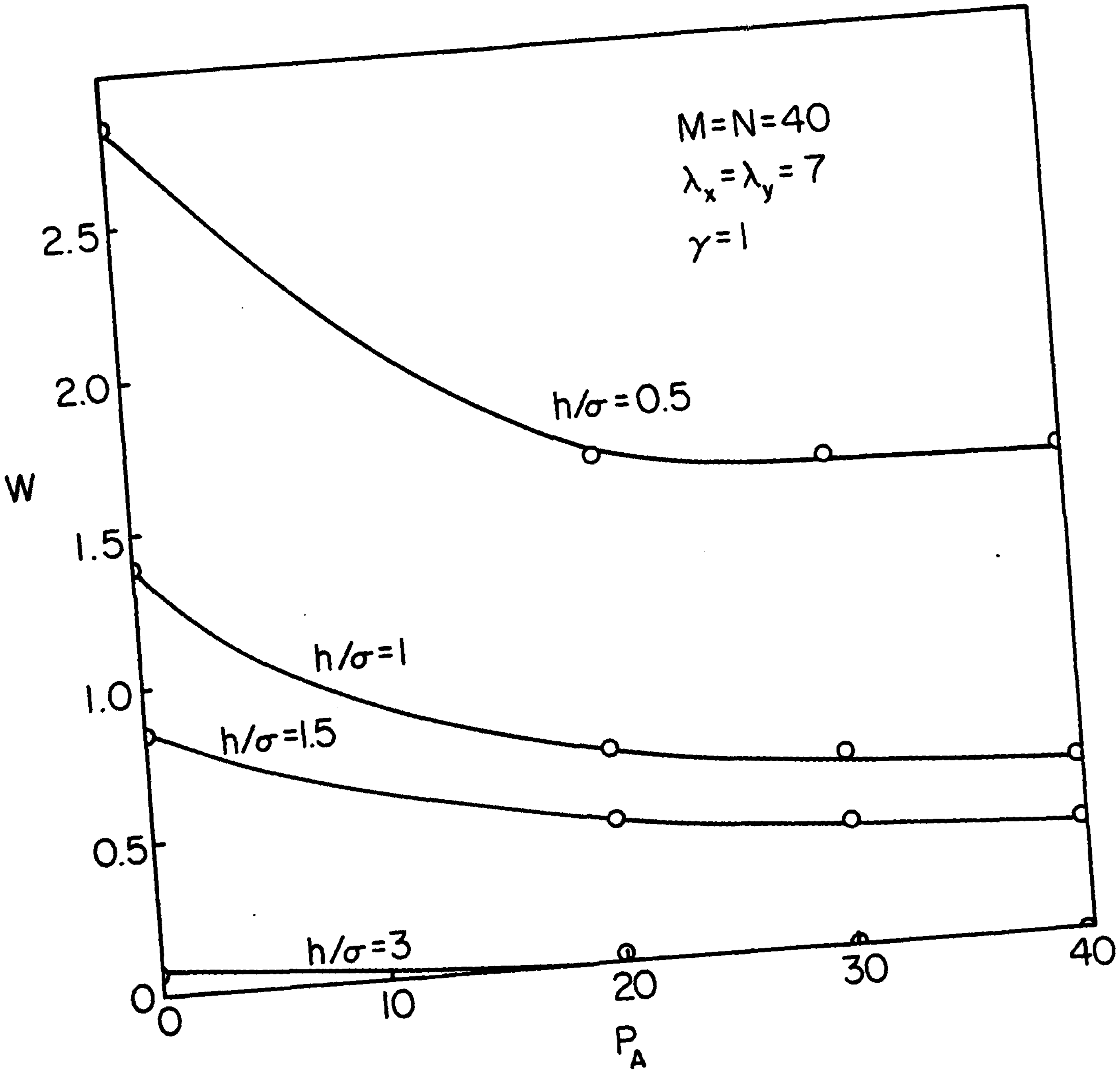

Figure 19. Change in load capacity by ambient pressure.

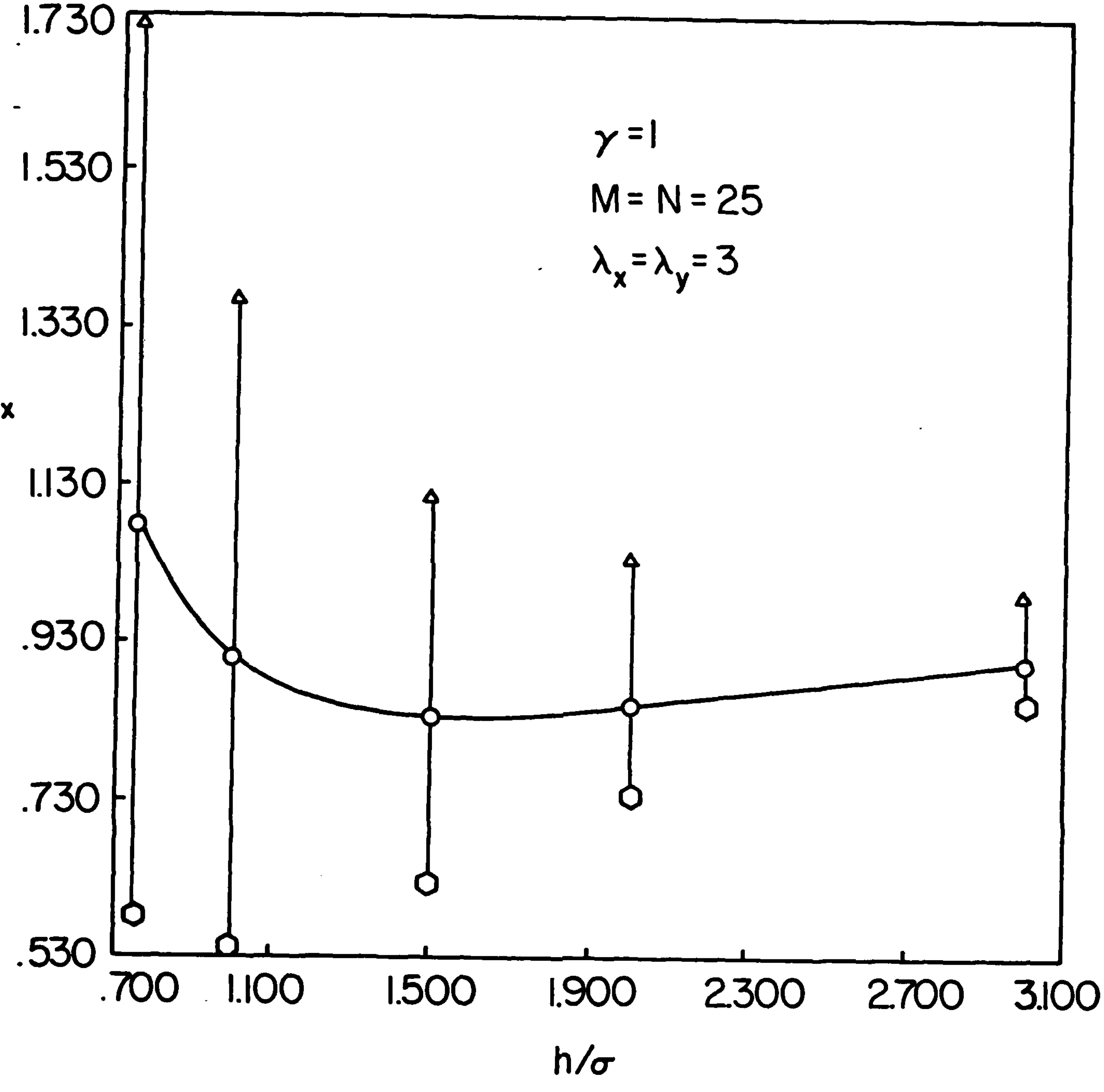

Figure 20. Scatter in pressure flow factor obtained from different but statistically identical surfaces.

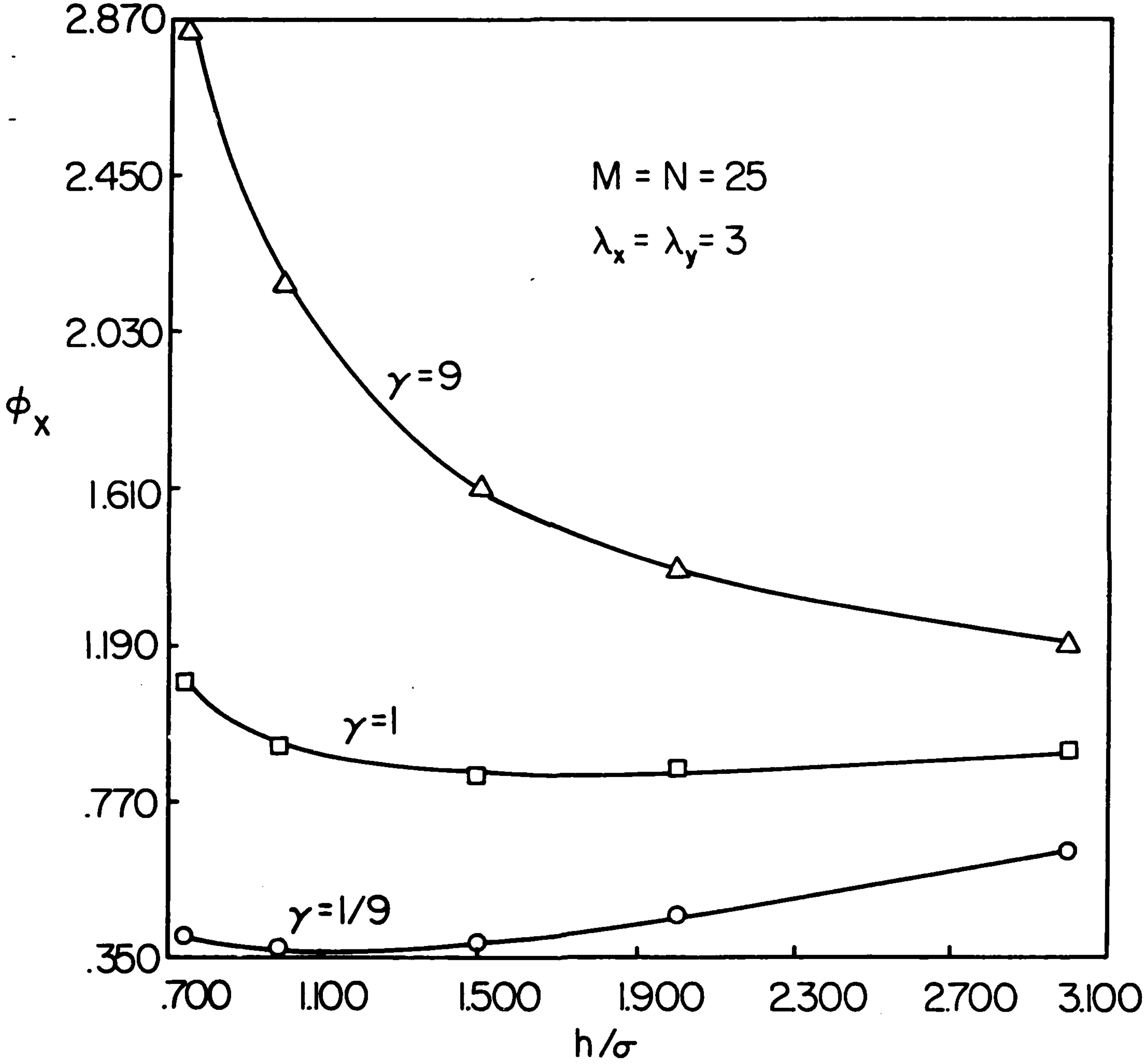

Figure 21. Pressure flow factor for Gaussian surfaces.

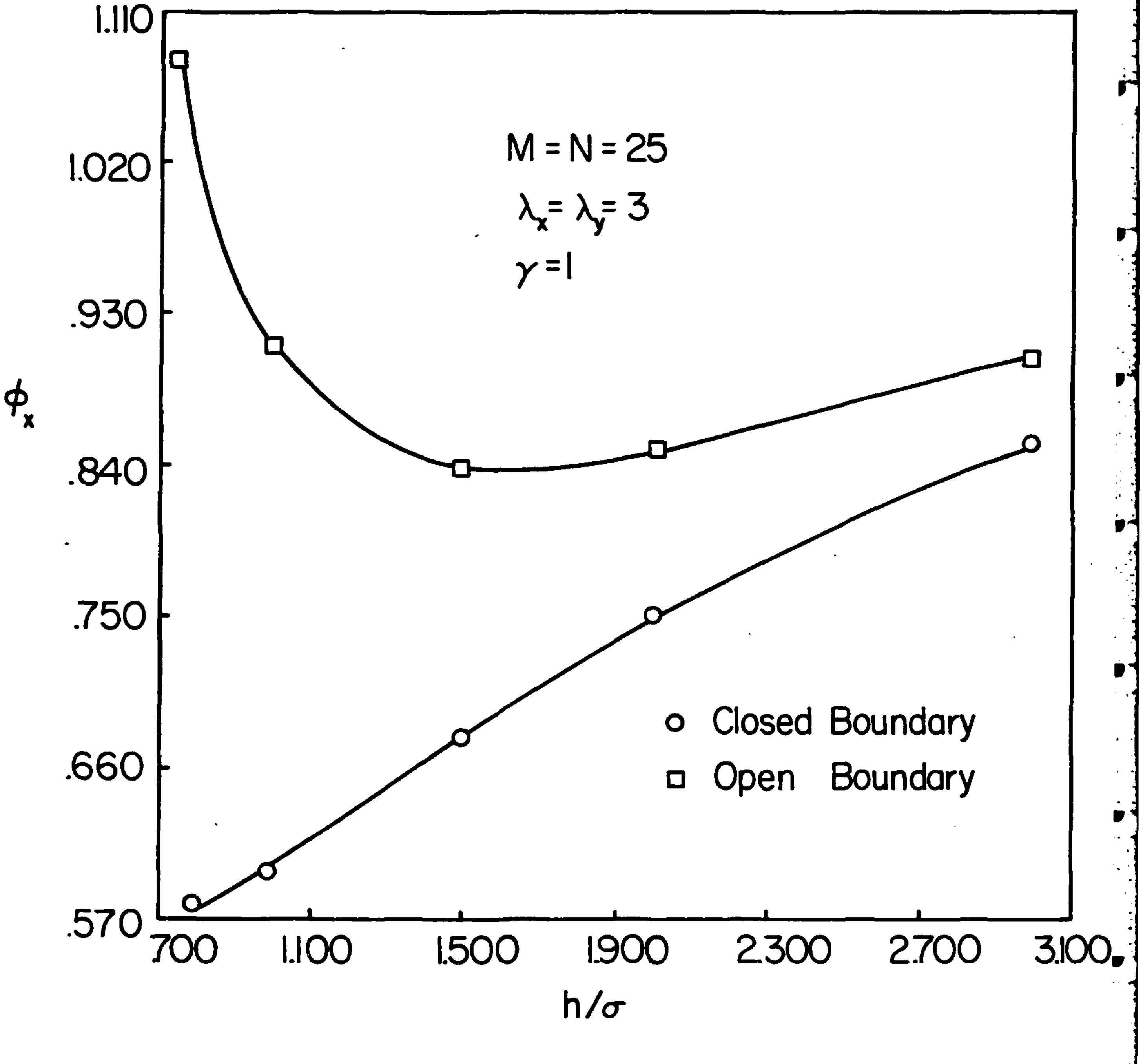

Figure 22. Comparison of pressure flow factor with Patir-Cheng Model.

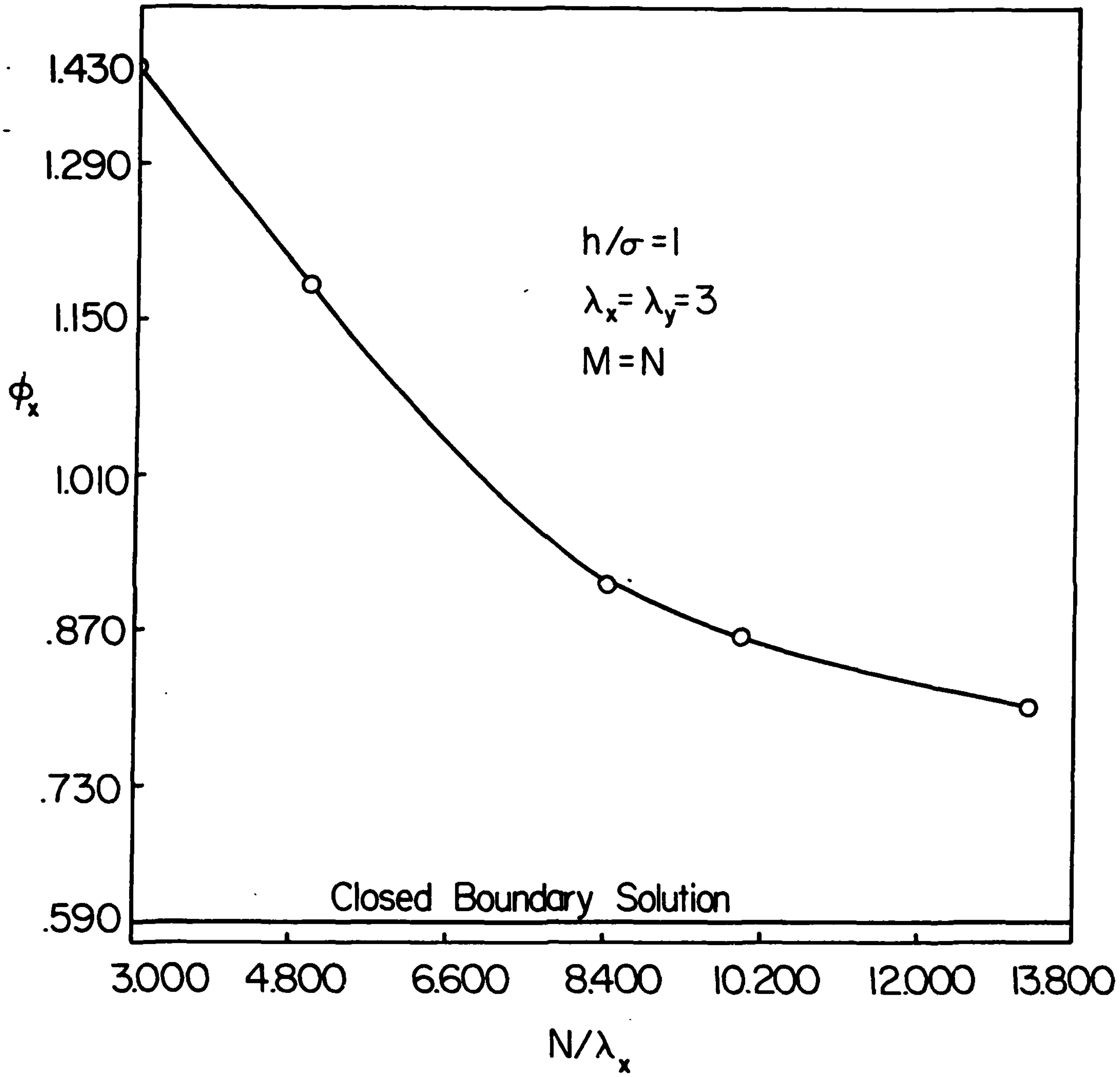

Figure 23. Change of pressure flow factor with number of asperities per simulation.

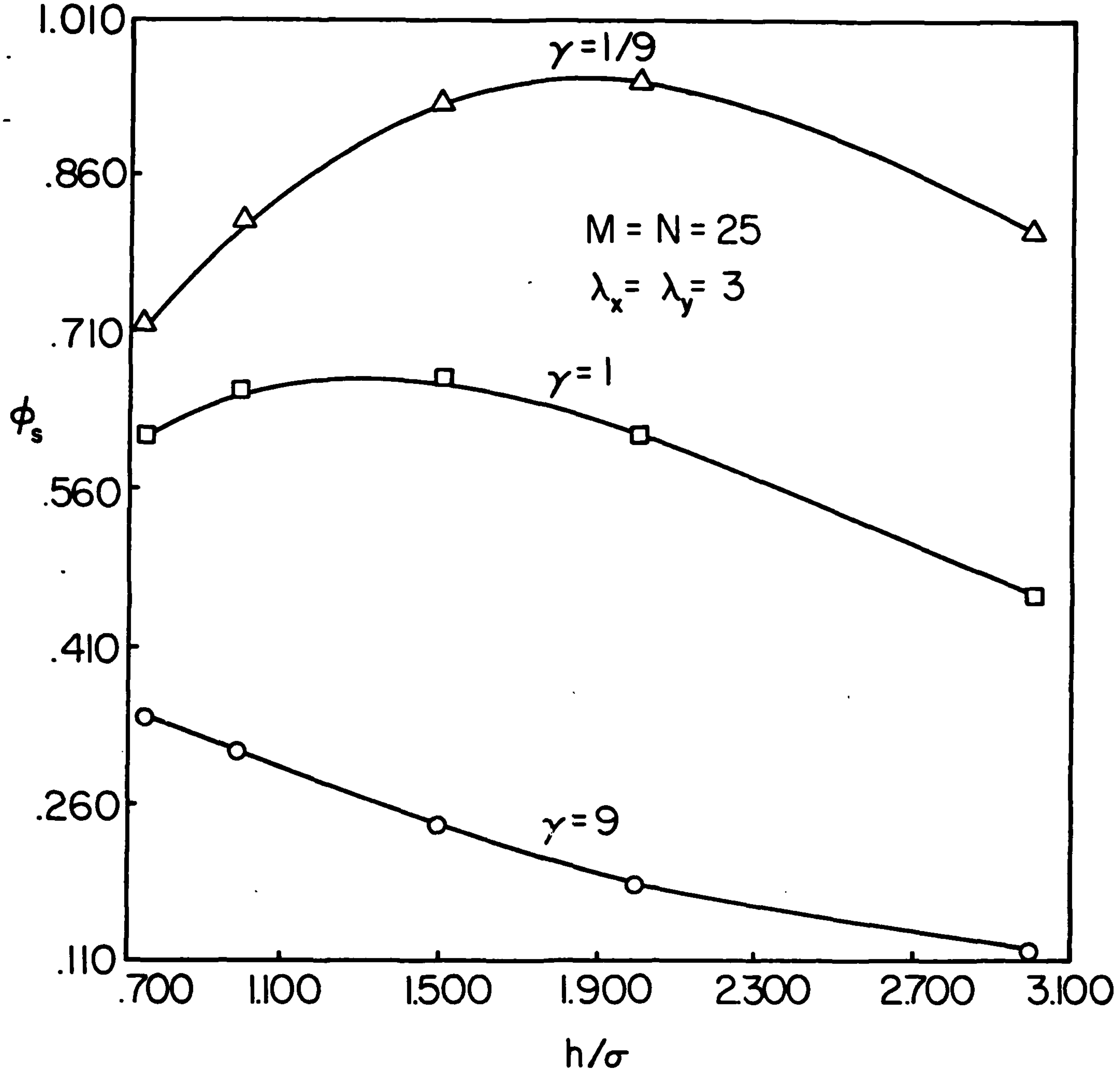

Figure 24. Shear flow factors for Gaussian surfaces.

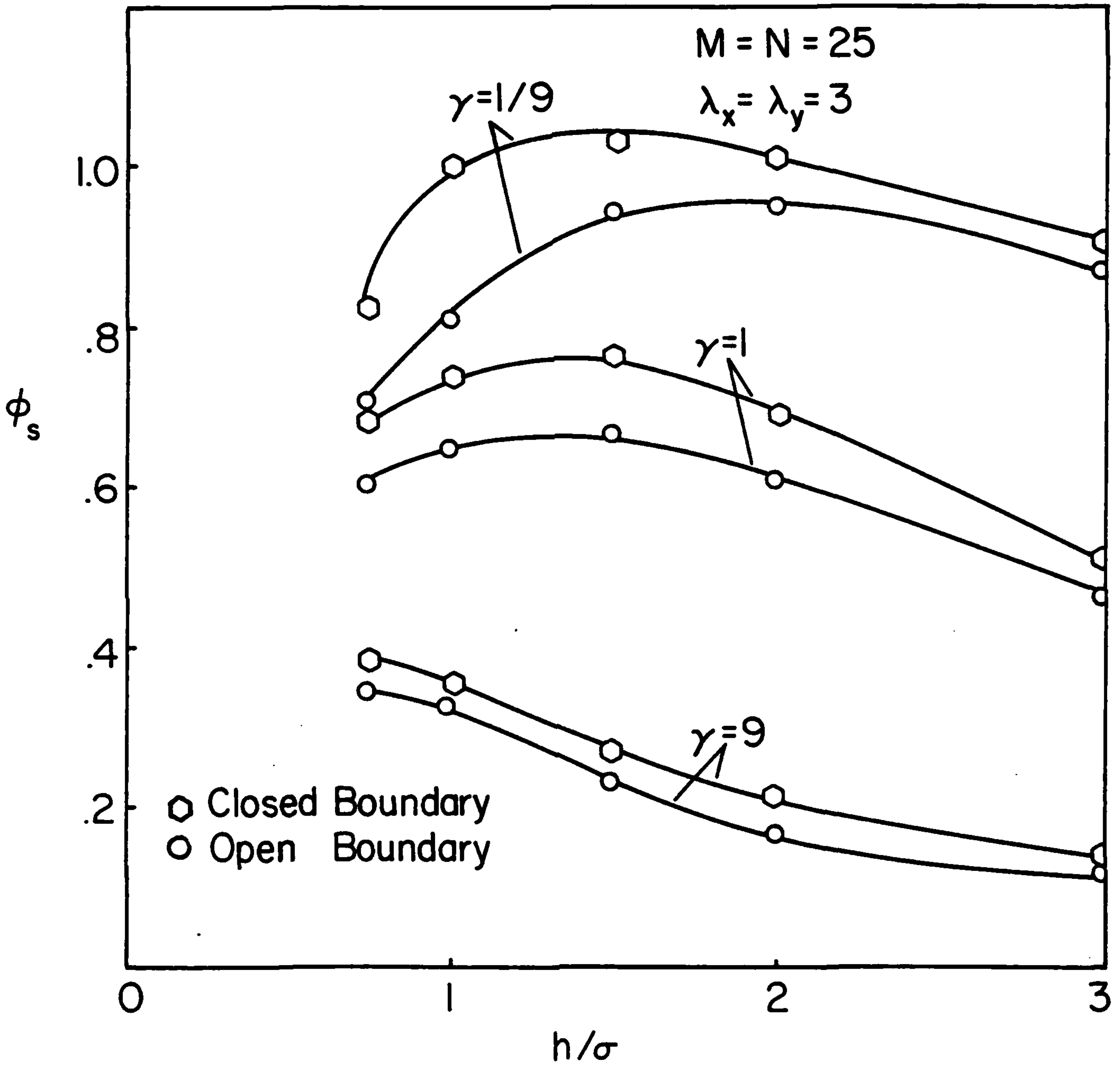

Figure 25. Comparison of shear flow factors with closed boundary model.

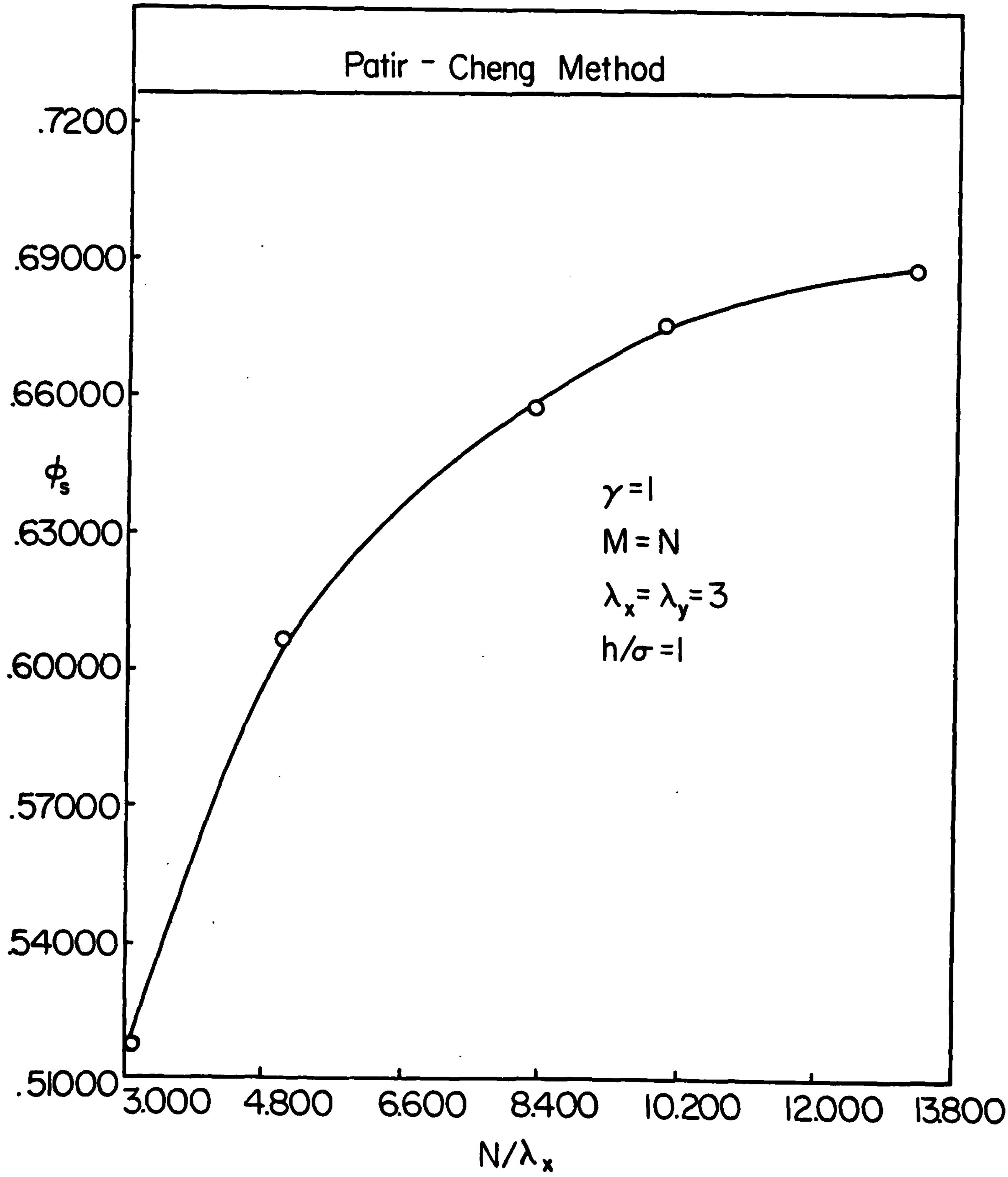

Figure 26. Change of ϕ_s with number of asperities in an element.

APPENDIX B

AVERAGE REYNOLDS EQUATION

For Reynold's roughness, a term given to roughness with small slopes, the average Reynold's equation

$$\frac{\partial}{\partial x}\left(\frac{h_T^3}{12\mu}\frac{\partial p}{\partial x}\right) + \frac{\partial}{\partial y}\left(\frac{h_T^3}{12\mu}\frac{\partial p}{\partial y}\right) = \frac{U_1+U_2}{2}\frac{\partial h_T}{\partial x} + \frac{\partial h_T}{\partial t} \qquad \text{A.1}$$

is applicable. Since most of the engineering surfaces are of that type of roughness, we assumed that local pressure in a rough bearing is governed by Equation A.1.

The mean pressure is usually the desired quantity in a bearing. However, since the H_T is a random quantity in Equation A.1, the local pressure is also a random quantity. Therefore, an average Reynolds equation is derived in terms of average film thickness and average pressure which governs the flow in a rough bearing.

Before deriving the average Reynolds equation, one should analyze the expected flows.

The local oil flows in a rough bearing are given by

$$q_x = -\frac{h_T^3}{12\mu}\frac{\partial p}{\partial x} + \frac{U_1+U_2}{2} h_T \qquad \text{A.2}$$

$$q_y = -\frac{h_T^3}{12\mu}\frac{\partial p}{\partial y} \qquad \text{A.3}$$

The film geometry randomly varies in a rough bearing. Therefore, the local oil flows are also random quantities. To obtain an average oil flow, consider an element with area ΔxΔy (Figure A.1). Note that this element should contain sufficient numbers of asperities and still should be small when compared with the dimension of bearing. In this case, the expected flow has small variances in this control volume. Therefore, they can be obtained by averaging along the length of the element. That is,

$$\bar{q}_x = E(q_x) = \frac{1}{\Delta y \Delta x} \iint_{y}^{y+\Delta y} q_x \, dydx \qquad \text{A.4}$$

$$\bar{q}_y = E(q_y) = \frac{1}{\Delta y \Delta x} \iint_{x}^{x+\Delta x} q_y \, dxdy \qquad \text{A.5}$$

where E is the expectancy operator.

In order to relate these mean flows to mean quantities like mean height and mean pressure, Patir-Cheng defined empirical factors such that expected unit flows are given by

$$\bar{q}_x = - \phi_x \frac{h^3}{12\mu} \frac{\partial \bar{p}}{\partial x} + \frac{U_1+U_2}{2} \bar{h}_T + \frac{U_1+U_2}{2} \sigma \phi_s \qquad \text{A.6}$$

$$\bar{q}_y = -\phi_y \frac{h^3}{12\mu} \frac{\partial \bar{p}}{\partial y} \qquad \text{A.7}$$

where $\bar{p}$ is the mean pressure and $\bar{h}_T$ is the mean gap.

In Equation A.6 the flow in x direction consists of three parts. The first term stands for the average flow due to the pressure gradient in x direction. The symbols ϕ_x and ϕ_y are called pressure flow factors, and can be thought as the correction factor between a rough and smooth bearing which has the same nominal geometry.

The second term in Equation A.6 represents the flow due to the entrainment velocity $(U_1 + U_2)/2$. This term is absent in Equation A.7 because there is no velocity in this direction.

The third term in Equation A.6 arises due to the combined effect of roughness and sliding. It represents the additional flow transport in the valleys of the rough surface. The ϕ_s term compares the flow in a rough bearing with a smooth one in case of sliding. The fluid carried in the valleys of the moving rough surface helps to transport the flow in the gap between the two surfaces. On the other hand, if a smooth surface is sliding against a stationary surface, the flow transport will be obstructed by the stagnant fluid in the valleys of the stationary surface. For this reason, the ϕ_s will be negative.

If we write down the mean flow balance on the control volume we obtain

$$\frac{\partial \bar{q}_x}{\partial x} + \frac{\partial \bar{q}_y}{\partial y} = - \frac{\partial \bar{h}_T}{\partial t} \qquad \text{A.8}$$

That is, the net flow leaving the volume is equal to net flow coming into the volume and the rate of change of volume.

Substituting Equation A.6 and A.7 into A.8, the following is obtained:

$$\frac{\partial}{\partial x}[\phi_x \frac{h^3}{12\mu} \frac{\partial \bar{p}}{\partial x}] + \frac{\partial}{\partial y}[\phi_y \frac{h^3}{12\mu} \frac{\partial \bar{p}}{\partial y}] = \frac{U_1+U_2}{2} \frac{\partial \bar{h}_T}{\partial x}$$

$$+ \frac{U_1+U_2}{2} \sigma \frac{\partial \Phi_s}{\partial x} + \frac{\partial \bar{h}_T}{\partial t} \qquad \text{A.9}$$

In order to calculate the mean pressure and mean flow, one should compute the flow factors first, as indicated in Chapters I and II. Flow factors have the properties

$$\phi_x, \phi_y \rightarrow 1 \qquad\qquad h/\sigma \rightarrow \infty$$

$$\phi_s \rightarrow 0 \qquad\qquad h/\sigma \rightarrow \infty$$

Derivation of ϕ_x and ϕ_y through simulation (Model problem 1):

In the previous section, it is assumed that the bearing consists of small, rectangular bearings with area δA_i and a constant nominal film thickness of h. The partitioned bearing approaches the geometry of the real bearing as the δA_i becomes smaller. However, δA_i should be large enough to contain sufficient number of asperities.

For each bearing pressure flow factors can be calculated by applying an arbitrary pressure flow on the boundaries of the element and solving pressure distribution and flow, then comparing it with the rough bearing with the same nominal geometry. Hence, evaluating for different nominal film heights ϕ_x and ϕ_y can be obtained as a function of h.

To obtain ϕ_x, Patir and Cheng (14) assumed $U_1 = U_2 = U$ (pure rolling) and considered the following model for simulation

$$\frac{\partial}{\partial x}\left[\frac{h_T^3}{12\mu}\frac{\partial p}{\partial x}\right] + \frac{\partial}{\partial y}\left[\frac{h_T^3}{12\mu}\frac{\partial p}{\partial y}\right] = \overline{U}\frac{\partial h_T}{\partial x} + \frac{\partial h_T}{\partial t} \qquad \text{A.10}$$

where $h_T = h + \delta_1 + \delta_2$ (see Figure A.1),

with boundary conditions (see Figure A.2):

1) $p = p_A$ at $x = 0$

2) $p = p_B$ at $x = L_x$

3) $p = (\frac{x}{L_x})\, p_B + (1 - \frac{x}{L_x})\, p_A \quad y = 0 \quad y = L_x$

4) no flow at contact points.

If we consider righthand side of Equation A.10, since h is constant within the element and $h_T = h + \delta_1 + \delta_2$

$$\overline{U}\,\frac{\partial h_T}{\partial x} + \frac{\partial h_T}{\partial t} = U\,\frac{\partial(\delta_1+\delta_2)}{\partial x} + \frac{\partial(\delta_1+\delta_2)}{\partial t} \qquad \text{A.11}$$

The δ_1 and δ_2 are time dependent due to the motion of the surface; therefore one can write them as

$$\delta_i = \delta_i(x - \overline{U}_t,\, y),\ i = 1.2 \qquad \text{A.12}$$

and

$$\frac{\partial \delta_i}{\partial t} = -\,U\,\frac{\partial \delta_i}{\partial x}, \qquad i = 1.2 \qquad \text{A.13}$$

Therefore, the righthand side of equation A.10 becomes

$$\overline{U}\,\frac{\partial h_T}{\partial x} + \frac{\partial h_T}{\partial t} = U\,\frac{\partial \delta_i}{\partial x} - U\,\frac{\partial \delta_i}{\partial t} = 0 \qquad \text{A.14}$$

Then, Equation 10 becomes:

$$\frac{\partial}{\partial x}\left[\frac{h_T^3}{12\mu}\,\frac{\partial p}{\partial x}\right] + \frac{\partial}{\partial y}\left[\frac{h_T^3}{12\mu}\,\frac{\partial p}{\partial y}\right] = 0 \qquad \text{A.15}$$

The δ_1 and δ_2 are randomly generated with known statistical properties, as outlined in Patir (15).

The pressure in the simulation element is solved using Equation A.15 and then ϕ_x is calculated using Equation A.6 and Equation A.5.

Since $U_1 = U_2 = U$, Equation A.6 becomes

$$\bar{q}_x = -\phi_x \frac{h^3}{12\mu} \frac{\partial \bar{p}}{\partial x} + U\, \bar{h}_T$$

After cancellation it becomes

$$\phi_x = \frac{\dfrac{1}{L_x L_y} \displaystyle\int_0^{L_y} \int_0^{L_x} \frac{h_T^3}{12\mu} \frac{\partial p}{\partial x}\, dydx}{\dfrac{h^3}{12\mu} \dfrac{\partial p}{\partial x}} \qquad \text{A.16}$$

where

$$\frac{\partial \bar{p}}{\partial x} = \frac{p_B - p_A}{L_x} .$$

The calculation of ϕ_y follows the same steps. The only difference is the flow in y-direction sees a different surface pattern than ϕ_x. That is, $\phi_x(h/\sigma), \gamma) = \phi_y(h/\sigma, 1/\gamma)$. Therefore, one should expect to get similar ϕ_x and ϕ_y values for isotropic surfaces.

Since pressure flow factors depend precisely on the roughness of each surface, in order to obtain a meaningful average one should solve the same problem for several times and average it.

Derivation of ϕ_s through simulation (Model Problem 2):

The shear flow factor, ϕ_s, is obtained by eliminating ϕ_x and ϕ_y from the equation A.8. Although there is a possibility of cavitation in a bearing when some sliding is introduced, this model problem does not consider that. This effect will be discussed in the following section in model problems.

To eliminate ϕ_x and ϕ_y from equation A.8, the rolling velocity is taken to be zero (i.e., $U_1 = U_2$). Then model problem for ϕ_s becomes pure sliding of two nominal surfaces:

$$\frac{\partial}{\partial x}\left[\frac{h_T^3}{12\mu}\frac{\partial p}{\partial x}\right] + \frac{\partial}{\partial y}\left[\frac{h_T^3}{12\mu}\frac{\partial p}{\partial y}\right] = \frac{\partial h_T}{\partial t} \qquad \text{A.17}$$

$$h_T = h + \delta_1 + \delta_2$$

$$U_1 = -U_2 = 1/2\ U_s$$

The boundary conditions are:

1) $P = p_A$ at $x = 0$, $x = L_x$

2) $p = p_A + C_1$ at $y = 0$, $y = L_y$

3) No flow at contacts.

To obtain flow factors, an infinitesimal displacement is induced on two surfaces and the pressure is solved.

Solving $\bar{q}_x$ from Equation A.9,

$$q_x = E\left(-\frac{h_T^3}{12\mu}\frac{\partial p}{\partial x}\right) = \frac{1}{L_xL_y}\int_0^{L_y}\int_0^{L_x}\left(-\frac{h_T^3}{12\mu}\frac{\partial p}{\partial x}\right)dxdy \qquad \text{A.18}$$

Since the mean pressure gradient is zero, and there is no rolling velocity, this expression is equal to the additional flow transport due to sliding:

$$\bar{q}_x = \frac{U_s}{2}\sigma\,\phi_s \qquad \text{A.19}$$

Combining A.19 and A.18, ϕ_s becomes

$$\phi_s = \frac{2}{U_s\sigma}\frac{1}{L_xL_y}\int_0^{L_y}\int_0^{L_x}\left(-\frac{h_T^3}{12\mu}\frac{\partial p}{\partial x}\right)dxdy \qquad \text{A.20}$$

Derivation of ϕ_s with effect of cavitation (Model Problem 3):

The shear flow factor is evaluated for cavitation using Equation A.17 of Model Problem 2 with different boundary conditions. It is assumed that the lubricant will cavitate the regions where the pressure is negative and the pressure will be equal to cavity pressure which is practically zero. The Model Problem 3 becomes the solution of Equation A.17 with boundary conditions:

(1) $p = p_A \qquad x = 0 \quad , \quad x = L_x$

(2) $p = p_A + C_2 \qquad y = 0 \quad , \quad y = L_y$

(3) $$p = \begin{matrix} p & \text{if } p > 0 \\ 0 & \text{if } p < 0 \end{matrix} \qquad \begin{matrix} 0 < x < L_x \\ 0 < y < L_y \end{matrix}$$

(4) No flow at contact points.

APPENDIX B

FINITE DIFFERENCE FORMULATION

The Reynolds equation for Model Problem 1 is non-dimensionalized as:

$$\frac{\partial}{\partial \bar{x}} [H_T{}^3 \frac{\partial p}{\partial \bar{x}}] + (\frac{L_x}{L_y})^2 \frac{\partial}{\partial y} [H_T{}^3 \frac{\partial p}{\partial y}] = 0 \qquad \text{B.1}$$

where

$$P = \frac{p-p_B}{p_A-p_B} \qquad H_T = \frac{h_T}{\sigma} \qquad \bar{x} = \frac{x}{L_x} \qquad \bar{y} = \frac{y}{L_y} \qquad \text{B.2}$$

Similarly, the Reynolds equation for Model 2 becomes:

$$\frac{\partial}{\partial \bar{x}}[H_T{}^3 \frac{p}{x}] + (\frac{L_x}{L_y})^2 \frac{\partial}{\partial y}[H_T{}^3 \frac{\partial p}{\partial y}] = \frac{\partial H_T}{\partial t^*} \qquad \text{B.3}$$

where

$$P = \frac{\sigma^2(p-p_A)}{6\mu U_s L_x} \qquad t^* = \frac{U_s t}{2L_x} \qquad \text{B.4}$$

and the Reynolds equation for Model Problem 3 becomes similar to Equation B.3 and B.4. However, since the pressure in Model Problem 3 is sensitive to nominal film thickness and asperity size rather than standard deviation of roughness σ^2 and bearing length L_x, the above expression for P is non-dimensionalized as

$$P_s = \frac{h^2(p-p_A)}{6\mu U_s L_x} \qquad \text{B.5}$$

where

$$L_x = \Delta x \lambda_x$$

and

$$P_s = \frac{H^2}{N\lambda_x}$$

The boundary conditions are similarly normalized. Since the lefthand side of the Equations B.1 and B.3 are the same, two problems can be solved simultaneously using the same coefficient matrix.

The finite difference equations for the two model problems can be written in the form:

$$G_{ij}P_{i-1,j}+E_{ij}P_{i,j-1}+D_{ij}P_{ij}+G_{i-1,j}P_{i+1,j}+E_{i,j+1}P_{i,j+1} = F_{ij} \qquad \text{B.6}$$

for $i = 1,2,\ldots,N$ $\qquad j = 1,2,\ldots,M$

where

$$G_{ij} = H_T^3{}_{i-1/2,j} \qquad E_{ij} = -H_T^3{}_{i,j-1/2}$$

$$D_{ij} = -(G_{ij} + G_{i+1,j} + E_{ij} + E_{i,j+1})$$

To obtain that form of equation both sides of the equation have been multiplied by $-(\Delta x)^2$ and the grids are chosen such that:

$$\frac{\Delta\bar{x}L_x}{\Delta\bar{y}L_y} = 1$$

that is

$$\Delta x = \Delta y$$

The coefficient matrix of the Equation 8.6 may be stored as symmetric banded matrix with Mx MN dimensions. The finite difference equation in matrix form becomes

$$[c][p] = [f] \qquad \text{B.7}$$

and can be solved by Gaussian elimination.

Then flow and shear flow factors can be obtained by numerical integration of Equations A.16 and A.20 of Appendix A.

To include no flow boundary conditions at contact points, the H_T at a half grid point is set equal to a small ε whenever its value is negative. Although the ε does not affect the pressure distribution through the bearing, it creates some pressure peaks under the contacts to avoid the pressure gradient created only due to the numerical reason, the flow is set equal to zero during the integration process to calculate flow factors. Another numerical problem arises when a pressure point surrounded by four contact points. To avoid this behaviour, these equations are helpful.

Finally, one should note that G and E in Equation B.6 are the third power of the heights at half-grid points. These heights at half-grid points cannot be obtained by averaging the heights at grid points since it is a random quantity. Therefore, heights should be generated at half-grid points as well.

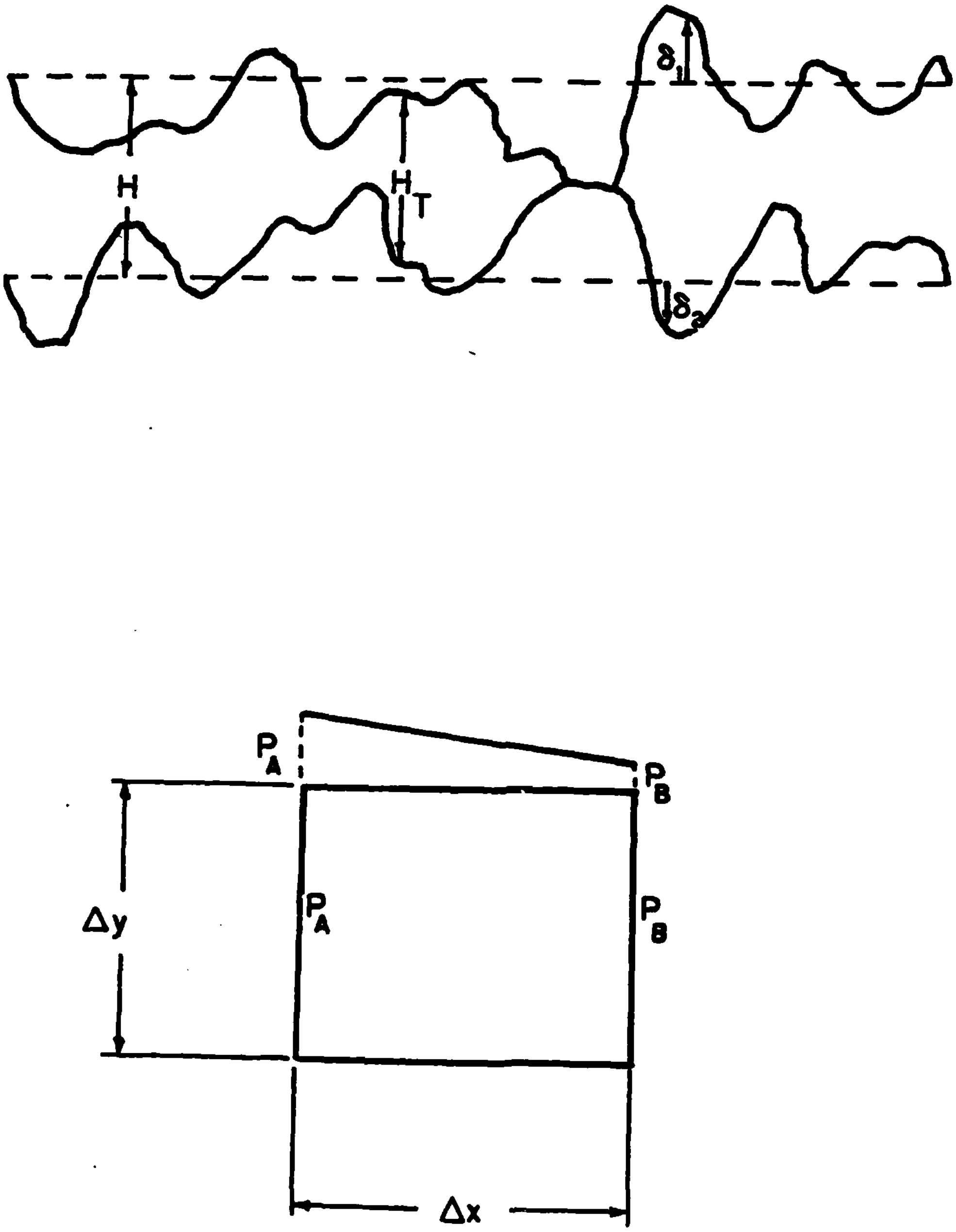

Figure A.1

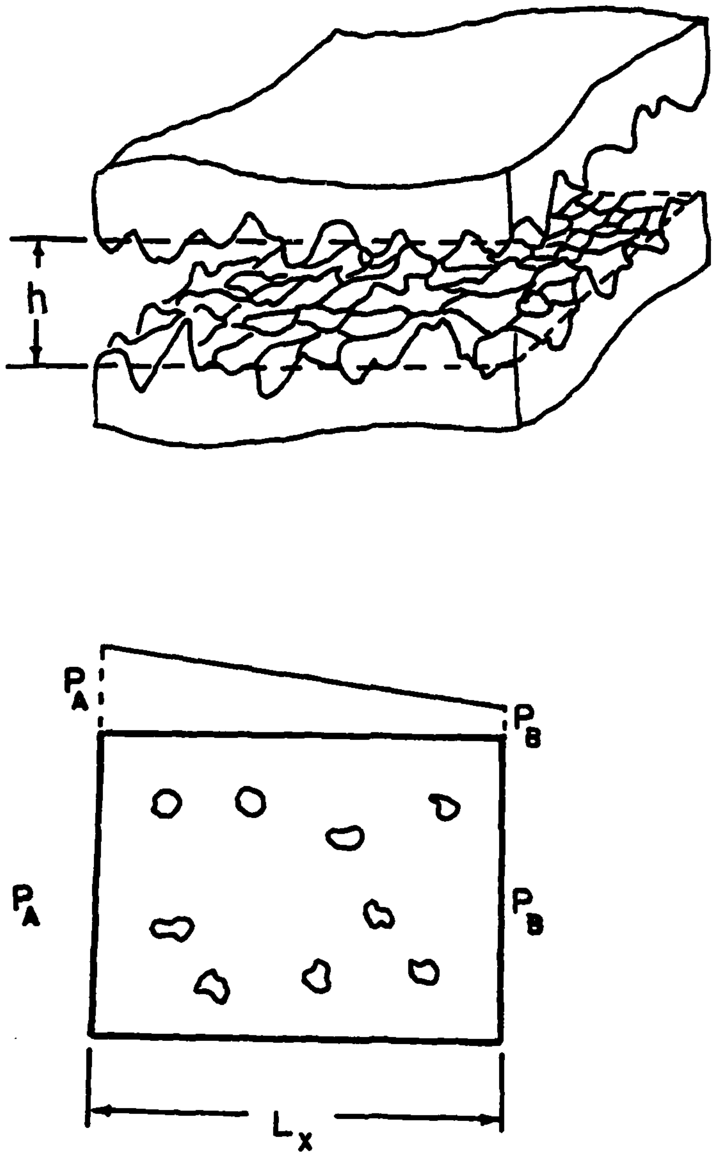

Figure A.2

END

FILMED

2-83

DTIC